© 2024. This manuscript version is made available under the CC-BY-NC-ND 4.0 license http://creativecommons.org/licenses/by-nc-nd/4.0/

Hydrodynamic analysis and optimization of a floating Wave Energy Converter with moonpool using OpenFOAM®

Muhammad Ahsan Khan[1], Gabriel Barajas[2], Maria Gabriella Gaeta[1], Javier L. Lara[2] and Renata Archetti[1,a)]

[1]*Department of Civil, Chemical, Environmental, and Materials Engineering, University of Bologna. Viale del Risorgimento, 2, 40136, Bologna, Italy.*
[2]*Instituto de Hidráulica Ambiental de la Universidad de Cantabria "IHCantabria". Parque Científico y Tecnológico de Cantabria. C/ Isabel Torres, Nº 15, 39011, Santander, Spain.*
[a)]*Author to whom correspondence should be addressed: renata.archetti@unibo.it*

Abstract

This paper presents the hydrodynamic analysis and optimization of a novel axisymmetric single cylindrical Wave Energy Converter (WEC) equipped with a moonpool, called MoonWEC. The primary aim of the study is to optimize the design of the MoonWEC by minimizing pitch rotations, enhancing heave motion, and facilitating moonpool oscillations. A set of new laboratory experiments was conducted to characterise the hydrodynamic response of the MoonWEC. These experiments were reproduced using a Numerical Wave Tank (NWT) in OpenFOAM. Qualitative and quantitative data were recorded, and the heave and pitch response was analysed by comparing experimental and numerical data. Good agreement between experimental and numerical data was observed throughout all the simulations. The results showed that the MoonWEC device can achieve the preferred excitation in heave, but it can also undergo the unpreferred excitation in pitch. By shifting the centre of mass, MoonWEC was numerically optimized to reduce the pitch rotations without affecting the heave oscillations. The moonpool motion was also analysed for the optimised prototype. The study shows that the CFD model in OpenFOAM coupled with the MooDy library can be used to simulate the hydrodynamics of the MoonWEC accurately. The optimization study shows that the centre of mass of the device is a key parameter in controlling the natural period of the device in pitch. The analysis of the moonpool shows that the MoonWEC has the potential to generate significant power.

Keywords: CFD; Numerical wave tank; Floating body; OpenFOAM; WECs; Wave-structure interaction; Moonpool

1. Introduction

In light of the burgeoning global energy demand and the escalating interest in the renewable energy sector, the scientific community has been drawn to develop sustainable and renewable energy resources to secure energy consumption, protect the environment and promote regional development (Mardani et al., 2015). In addition to the widely commercialized solar and wind energy sources, oceans have emerged as an alluring prospect due to their significant potential in the field of renewable energy. This potential encompasses a diverse array of energy forms, including wave, tidal, current, and ocean thermal energy conversion. Wave energy (density 2-3 kW/m^2), which is denser than wind (density 0.4-0.6 kW/m^2) and solar energy (density 0.1-0.2 kW/m^2) (Erdinç et al., 2015), is still in its first stages of development and commercialization. It is harnessed through the deployment of Wave Energy Converters (WECs) and is a very constant energy source as WEC devices can generate power up to 90% of the time, compared to 20-30% for wind and solar power devices (Pelc and Fujita, 2002; "Power buoys", 2001). Floating WECs are a particularly better option for exploiting offshore wave resources, as they can be deployed in deeper waters and harvest greater amounts of energy (Duckers, 2004). They also have a lower visual impact on the ocean views, as they can be installed kilometres away from the coasts (Barooni et al., 2022). WEC devices have a limited negative environmental impact in use, with offshore devices having the lowest potential impact (Thorpe, 1999; Drew et al., 2009).

The efficient development of an economically competitive wave energy technology relies on early-stage assessment, optimisation, and refinement of the system design using numerical methods (Weber et al., 2013). Predicting the performance of WECs and their response to wave interaction is strictly dependent on good modelling of wave action and hydrodynamic characteristics (Zabihi et al., 2017). Numerical Wave Tanks (NWTs) provide an excellent numerical tool for the research and development of WECs, offering a cost-effective platform for their experimentation, analysis, and optimisation (Davidson et al., 2019).

Experimental tests of complex three-dimensional (3D) floating structures can be time-consuming and expensive. Numerical modelling is a complementary method to effectively study similar processes. It is significantly less expensive

than physical testing and can be used for various purposes, such as a method to describe the hydrodynamics around a structure in advance, illustrate the regions of interest, identify the most appropriate locations for mounting measuring devices, or even identify the most important scenarios for physical testing. Despite the good performance of potential flow models in predicting hydrodynamics for floating bodies, certain non-linear extreme processes are not well reproduced due to the strong assumptions of this framework. Recent developments in computational power have enabled the development of fully nonlinear Computational Fluid Dynamics (CFD) models that solve the Navier-Stokes equations to calculate nonlinear wave loads.

The advantage of CFD is its ability to accurately solve fluid motion, which is extremely difficult for most engineering flows of interest. However, setting up the numerical strategy requires several choices and parameter selection. For example, the turbulence model (Li and Fuhrman, 2022), the optimum mesh size (Eskilsson et al., 2017), and the model to reproduce the behaviour of mooring lines (Chen and Hall, 2022) are just a few of the many fundamental aspects of the simulation. The generation and resolution of the mesh and the definition of appropriate boundary conditions can be challenging when using a CFD model. A high mesh resolution is often required for a stable and accurate solution. This means that CFD modelling can be computationally expensive. Additionally, with current computing systems, accurate CFD models can require simulation periods of several days or weeks for near-field dispersion and mixing. There is a trade-off between model stability, the accuracy of the numerical solution, and computational cost. These choices can significantly impact the estimation of the modelled phenomenon. However, once developed, calibrated, and validated, CFD models can be a valuable tool to cross-check any physical phenomenon or even generate high-resolution 3D views.

In addition to commercial software packages, open-source CFD software has become increasingly popular and is often supported by active communities due to its free license and open-source code. A prime example of such an open-source CFD package is Open-source Field Operation And Manipulation, commonly known as OpenFOAM® (OpenFOAM® User Guide; Jasak, 1996; Rusche, 2002).

The ability of OpenFOAM to simulate the hydrodynamic response of floating rigid bodies has been demonstrated in recent literature. Palm et al. (2016) performed CFD simulations to model the dynamic behaviour of a WEC exposed to waves using the mesh morphing method in OpenFOAM. Islam et al. (2019) also used the morphing technique to simulate the wave-induced motion of a floating barge. Peng et al. (2023) studied the wave attenuation performance and motions of a floating breakwater utilizing the mesh morphing method. Sjökvist and Göteman (2016) studied peak forces on a WEC in extreme waves using an experimentally validated NWT, developed in OpenFOAM. Di Paolo et al. (2018) used the overset framework to compare the numerical model predictions with laboratory data for a floating pontoon anchored to the bottom and interacting with waves and currents. Chen et al. (2019) developed an NWT by incorporating the overset mesh methodology in OpenFOAM to analyse two-dimensional (2D) regular waves interacting with a floating cylinder and box-shaped body, and the heave decay of a point absorber WEC. Benites-Munoz et al. (2020) used the overset technique to simulate a WEC rotating at a large angle and observed good agreement with experiments. Wu et al. (2021) dynamically simulated small floating bodies that may resemble isolated small ice floes using the overset technique.

To evaluate the overset mesh method for control studies of WECs in an OpenFOAM NWT, Windt et al. (2020) presented a detailed comparison of the overset and mesh morphing methods, employing several test cases of increasing complexity. They found that the mesh morphing simulation crashes when the device motion becomes large and that the runtimes for overset mesh simulations are approximately double the time required for the mesh morphing simulations. Katsidoniotaki and Göteman (2022) also used the overset method and compared it with the mesh morphing method. They reached the same conclusion, finding that the two methods provide equivalent results when stable, but that the latter is susceptible to mesh deformation and fails to proceed with the simulations.

One of the key challenges in wave-structure interaction (WSI) for floating bodies is to reduce computational costs while supporting wave propagation without excessive damping. Several authors (Palm et al., 2016; Chen et al., 2019; Pinguet et al., 2022; Katsidoniotaki and Göteman, 2022) define a mesh refinement around the free surface and create zones far from the structure with larger cell sizes to reduce computational costs. Other authors (Chandar, 2019; Chen and Hall, 2022; Brown et al., 2021; Barajas et al., 2022) do not use mesh refinement. Computationally, mesh refinement is very efficient, but it can lead to unstable simulations for complex geometries under several conditions, such as when analysing survivability conditions. Therefore, mesh refinement around the free surface is not used in the current study.

Researchers are also investigating the use of mooring systems in NWTs. The mooring toolboxes MooDy (Palm et al., 2017; Palm, 2017; Palm and Eskilsson, 2018), a finite element mooring model, and MoorDyn (Hall, 2020), a lumped-mass mooring model, are both compatible with OpenFOAM. A comparison study by Chen and Hall (2022) found that the

accuracies of these two toolboxes are fairly similar, as they validated a coupled model against experimental measurements for a floating box moored with four catenary lines subjected to regular waves. In another study, Aliyar et al. (2022) applied a coupled solver to simulate the interaction of sea waves with the substructure of the Floating Offshore Wind Turbine (FOWT) platform to study the survivability of floating structures in extreme sea states. The mooring lines were modelled by considering them as a linear spring with defined spring stiffness in OpenFOAM and also by coupling an OpenFOAM solver (foamStar) with MoorDyn. Chen et al. (2022) investigated the wave dissipation performance of a floating box-type breakwater under a long-period wave using 2D numerical wave flume simulations in OpenFOAM. They used the MooDy library to simulate the mooring lines. In a study by Barajas et al. (2022), MooDy in the overset framework in OpenFOAM is used to model the motions of a WEC under constant waves.

Recently, the University of Bologna patented a WEC concept, called MoonWEC (Miquel and Archetti, 2019; Miquel and Archetti, 2020; Miquel et al., 2020). Inspired by the OXYFLUX device (Antonini et al., 2012; 2015; 2016a; 2016b), whose primary function is to pump well-oxygenated surface water to the bottom, MoonWEC is a novel hybrid WEC device that enables energy conversion from short-period waves. It was granted a patent due to several features that distinguish it from existing concepts. The European Patent Office (EPO) recognized the concept shape as the main novelty, which includes a ballast disc at the bottom and a conical shape at the top. WECs can be classified according to their energy conversion principles, technology, location and other characteristics (Falcão, 2010). Point absorbers are WECs with relatively small dimensions compared to the wavelength of the incident waves (Guo et al., 2022). MoonWEC combines the properties of a point absorber and an oscillating water column (OWC) to harvest energy from the relative motion between the floating structure and the moonpool, which is typically a cylindrical water column located inside the floating structure. In a study by Aalbers (1984), the relative motion between the moonpool surface and the floating structure in heave was observed under various conditions. The water column is assumed to behave like a frictionless piston with a mass that varies proportionally to its position. A comprehensive description of the MoonWEC concept, its novelty, and preliminary modelling using a potential flow model is presented by Miquel et al. (2020).

Moonpool-based devices have also been studied in the context of wave energy conversion by multiple authors. Jiang et al. (2017) used CFD to investigate fluid resonance in a moonpool by rectangular hulls in heave. Their study was limited to the moonpool simulations using a fixed mesh without considering rigid body dynamics and the mooring system. Tan et al. (2021) investigated the damping of wave-induced resonant oscillations of a moonpool between two fixed boxes using physical model testing and a modified potential flow model. Mia et al. (2023) used 2D CFD simulations to analyse the effects of heave motion on wave energy harvesting efficiency for an elastically supported floating OWC device with an air chamber at the top. They validated the numerical model using experimental data and then used the model to analyse the effect of the natural frequency on the hydrodynamic efficiency of the OWC. Göteman (2017) modelled a farm of cylindrical floats with a moonpool using the potential flow model in WAMIT. Sheng et al. (2012) and Singh et al. (2020) presented experimental studies on floating cylinder OWC WEC with an air chamber at the top. Alves et al. (2010) reported a numerical study using a 3D radiation-diffraction panel model, based on the classic linear water wave theory and potential flow, for a floating WEC device with an internal OWC. 2D wave-induced fluid oscillations in two narrow gaps were numerically investigated by Song et al. (2022) and the hydrodynamic performance of two heaving OWC devices separated by a gap was evaluated by Wang et al. (2022), both using potential flow models. Jiang et al. (2021) investigated wave resonance in a narrow gap formed by two boxes in the side-by-side arrangement by using an NWT based on OpenFOAM.

All the studies reviewed above involve moonpool modelling, however, none of these studies employ a coupled CFD model in OpenFOAM with a dynamic mesh and dynamic mooring library simultaneously. This gap in the literature presents an opportunity to investigate the coupled dynamics of moonpool-based WECs, such as MoonWEC, with their mooring systems using a high-fidelity CFD model in OpenFOAM.

The main objective of this study is to analyse and optimize the hydrodynamic response of MoonWEC using physical experiments and numerical simulations in OpenFOAM coupled with the MooDy library. The coupled CFD model is validated against laboratory experiments and then used to optimize the hydrodynamic response of the device by varying its physical properties. The study presents original experiments, including free decay and WSI tests, conducted at the University of Bologna on a small-scale prototype of MoonWEC. Parametric simulations, by varying the centre of mass, have been carried out to investigate the importance of this parameter on the heave and pitch motion of MoonWEC. The amplification of the moonpool is also demonstrated for an optimal configuration of the prototype. Overtopping effects are not quantified in either the experiments or the numerical simulations, which is a limitation of the present work.

The paper is structured as follows: following the introduction in Section 1, Section 2 provides a brief description of the MoonWEC device. Section 3 presents the original laboratory experiments in the wave flume, which are used to validate the CFD model. Section 4 describes the numerical setup. Section 5 provides the validation of the CFD model using the free decay and WSI tests. Section 6 presents the study of the device motion for three virtual MoonWEC prototypes with different mass properties using the validated CFD model. Finally, Section 7 provides concluding remarks.

2. MoonWEC device

MoonWEC (Miquel and Archetti, 2020) is a patented WEC device, which is named after its main structural element, a moonpool. It comprises two physical bodies before deployment in water: a floating structure and a Wells turbine. The floater has a hollow cylinder with a disc at the bottom, which forms a third virtual body, the moonpool, when placed in water.

In MoonWEC, both the floater and the moonpool are excited by wave action. The heave motion of MoonWEC is of prime importance and must be amplified. The motion of the moonpool relative to the floater is also very important in the MoonWEC concept as energy conversion is achieved by exploiting their relative motion. Therefore, the motion of the moonpool itself should also be amplified. The moonpool acts as a deformable body and can reach a resonant state if well-tuned.

The dimensioning of the MoonWEC, as described by Miquel et al. (2020), depends on the moonpool. A floating structure can be simplified as a mass-spring-damper system (Barreia et al., 2005). As such, if properly excited with a given frequency, it produces a resonant state. This frequency, known as the system's natural frequency, is associated with:

$$\omega_0 = \sqrt{\frac{k}{m}} \tag{1}$$

Where k is the system's elasticity constant, and m is its total mass. The parameters k and m may not be constant for complex geometries, as the elasticity can vary with hydrostatics and the mass with the added mass due to wave radiation. Nevertheless, its derivation is straightforward for the moonpool in heave mode (Sphaier et al., 2007). Because of its simple cylindrical structure, it is possible to simplify Equation (1) to:

$$\omega_0 = \sqrt{\frac{g}{d}} \tag{2}$$

Where g is the acceleration due to gravity and d is the draft of the moonpool. For example, if the moonpool has to resonate for sea states with a peak period (T_p) of 6 s (for the selected locations of Alghero and Mazara del Vallo in the Italian Mediterranean Sea), the draft of the moonpool, and therefore the draft of the structure, is directly yielded to be 9 m. Thus, the floater's total height is estimated to be equal to 10 m, giving the conical portion a freeboard of 1 m. The conical upper shape is intended to enhance the structure's amplitude motion. Such a shape could also stimulate the overtopping effect by acting as a ramp for waves to climb up and discharge a certain amount of water into the moonpool. For this reason, the MoonWEC device is a hybrid WEC, being a point absorber, a floating oscillating water column and an overtopping device. The Wells turbine handles energy conversion in MoonWEC, which is placed inside the moonpool. The layout of the device is presented in (Miquel and Archetti, 2019) and is shown here in **Fig. 1**. **Table 1** presents its characteristics on a real scale.

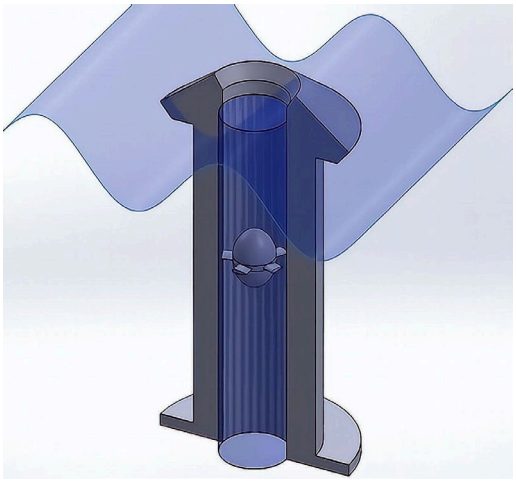

Fig. 1. MoonWEC layout showing the floater section, Wells turbine, and moonpool (Miquel and Archetti, 2019).

Table 1. *Characteristics of MoonWEC on a real-scale* (Miquel and Archetti, 2019).

Parameter	Value
Depth (m)	50
MoonWEC diameter (m)	5
Structure height (m)	10
Structure draft (m)	9
Structure Mass (ton)	150
CoG (m)	4.3
Moonpool diameter (m)	2.2
Wells turbine profile (-)	NACA0021
Wells turbine solidity (-)	0.47
Wells turbine hub-to-tip ratio (-)	2/3
Wells turbine chord length (m)	0.5
PM generator nominal power (kW)	50
Mooring wire type (-)	Six Strand
Mooring wire diameter (mm)	75
Mooring wire length (m)	150
Anchor point (m)	120

The MoonWEC device is moored to the seabed using a catenary system commonly referred to as the CALM (Catenary Anchor Leg Mooring) system. It is moored by four catenary lines, providing a strong symmetric behaviour with respect to the vertical plane. The CALM system is particularly suitable when it is necessary to reduce horizontal displacement. The MoonWEC device is moored using the CALM system because it is appropriate for heaving WECs, as it mainly blocks horizontal displacements while releasing free the vertical oscillations, and thus does not interfere with the motion of energy conversion. For further details on the MoonWEC device, please refer to Miquel et al. (2020).

3. Laboratory experiments

Laboratory experiments on a small-scale prototype of the MoonWEC device were conducted at the Laboratory of Hydraulics Engineering at the University of Bologna. The laboratory campaign was designed to create simple experiments that would preserve the main characteristics of MoonWEC while simplifying the study and providing an accurate analysis of the device. Therefore, two sets of experiments were performed to characterize the prototype's behaviour in a 3D interaction. First, a free decay test was conducted to measure the prototype's natural period in heave. Second, six WSI tests were conducted to analyse and quantify the heave motion when the device interacts with regular waves. The experiments were used later to validate the NWT in order to perform a parametric study on the MoonWEC device.

3.1 Experimental setup

The experiments were performed in the 15 m x 0.5 m x 0.7 m experimental wave flume, shown in **Fig. 2**. Each panel of the wave flume is 1 m long. The maximum water depth used for the current experiments was 0.4 m. The waves were

generated on the left-hand side of the flume by the vertical movement of a cuneiform-shaped piston-type wave-maker. A wave absorber panel on the right-hand side of the flume was used to minimize wave reflection.

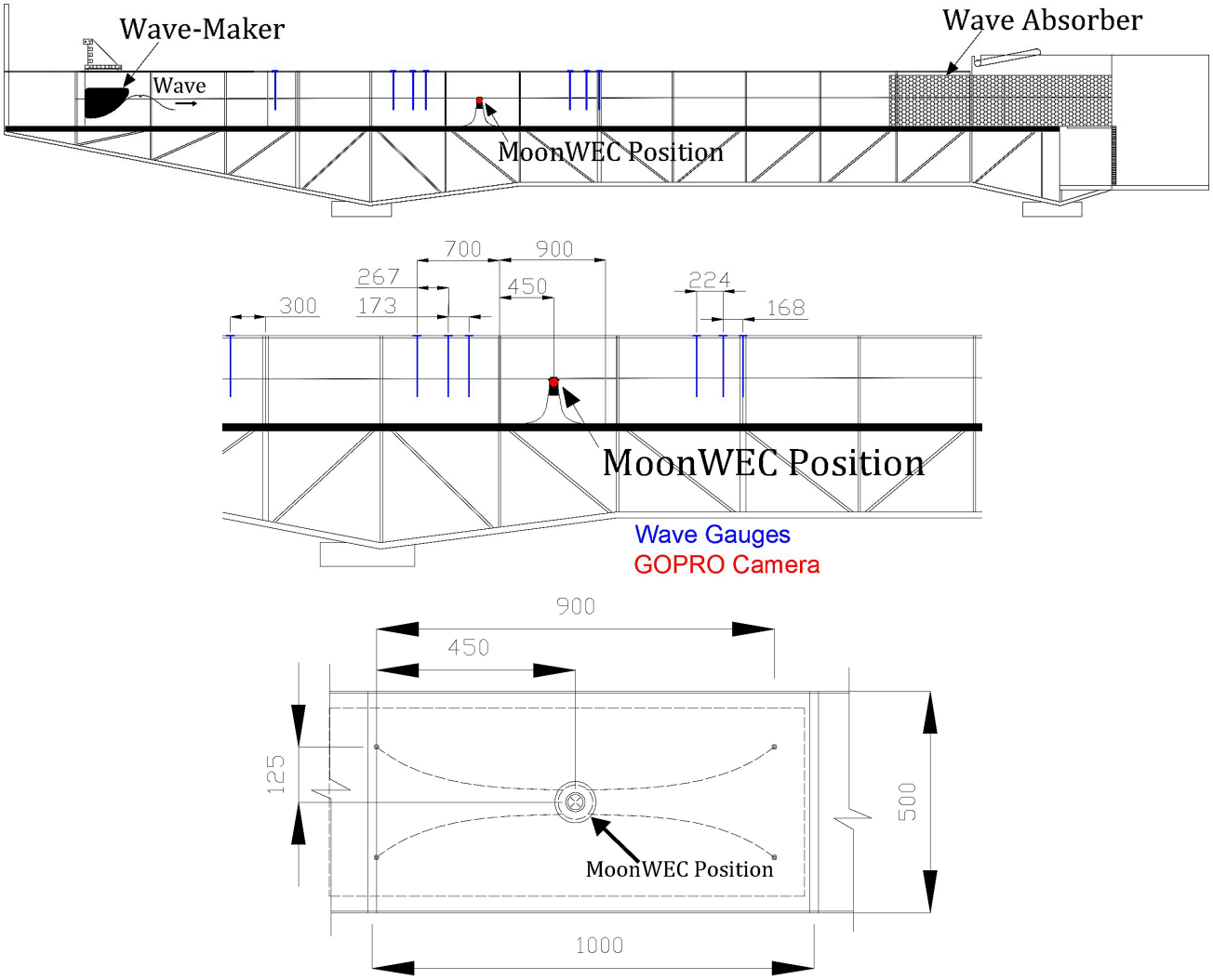

Fig. 2. Front view of the experimental wave flume (top); partial front view of the wave flume with MoonWEC and wave gauges position (middle); partial top view of the experimental wave flume with MoonWEC and the mooring anchor points' position (bottom) (all distances are in mm).

3.2 MoonWEC prototype

The MoonWEC prototype, shown in **Fig. 3**, was reproduced on a scale of 1:64 as a hollow wooden cylinder with its axis coincident with the structure's vertical axis. A brass disc was attached to the bottom of the cylinder as a damping disc to introduce a phase lag between the floating structure and the moonpool oscillatory motions. The Wells turbine was not considered in the current study.

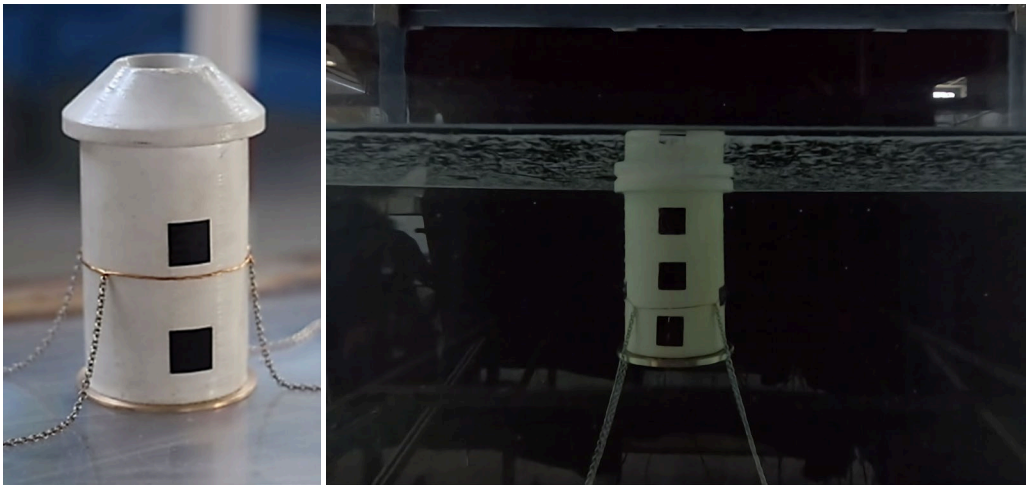

Fig. 3. Left panel: MoonWEC prototype outside the experimental wave flume, right panel: MoonWEC prototype deployed in the experimental wave flume with control points on its surface.

The use of a reduced scale for the MoonWEC prototype in the laboratory experiments is justified by extensive research on the scale effect in studies of floating cylinders and spar platforms under the action of surface waves (Ran et al., 1996; Utsunomiya et al., 2013; Wang and Zhou, 2020). Adoption of Froude similarity law in the laboratory inevitably entails the distortion of forces, such as surface tension (Weber number) and viscosity (Reynolds number). Incorrect scaling of surface tension can affect the dynamics and the type of wave breaking (Stagonas et al., 2011), but in our experiments, wave breaking was not present and, overall, no significant effect of reduced wave energy dissipation at the wave-structure interaction was observed when compared to computations. A distorted representation of the fluid viscosity leads to lower Reynolds numbers and larger viscous forces in the model tests (Altomare and Gironella, 2014), which could lead to overestimating drag coefficients and consequently higher loads on the objects and smaller wave transmission at real scale (Wang and Zhou, 2020). A full-scale installation of MoonWEC in the open sea will likely imply an increase in friction effects due to salinity, plant growth, suspended sediments, etc. These effects can only be studied for a large-scale prototype installation in the sea, which is typically the last step of research for WEC devices (Vissio, 2017) and cannot be included in laboratory experiments.

The mooring system was made up of four lightweight metal chains to control the directional heading of the MoonWEC prototype. The chains were attached to the MoonWEC floater at a height equivalent to its centre of mass and are spaced 90° apart along the circumference. The positions of the MoonWEC prototype, wave gauges, and mooring anchor points in the wave flume are shown in **Fig. 2**. The prototype is moored at its equilibrium position, 4.5 m away from the wave-maker. **Table 2** presents the characteristics of the reduced-scale prototype used in the experiments, including the mooring chains. **Fig. 4** shows the sketch of the prototype with the centre of mass (CoM) and centre of buoyancy (CoB), as calculated from its CAD model in SolidWorks®.

Table 2. *Characteristics of the reduced-scale MoonWEC prototype with mooring chains.*

Parameter	Value
Total height including bottom disc (mm)	156.25
Floater internal diameter (mm)	34.38
Floater external diameter (mm)	78.12
Bottom disc internal diameter (mm)	34.38
Bottom disc external diameter (mm)	90.00
Bottom disc thickness (mm)	4.00
Centre of Mass (CoM) (mm)	(x, y, z) = (0.00, 0.00, 51.62)
Centre of Buoyancy (CoB) (mm)	(x, y, z) = (0.00, 0.00, 72.09)
Draft (mm)	135 (measured from the bottom)
Total mass (g)	527.54
Mooring chain length (mm)	620
Mooring chain weight per unit length (g/m)	11.5
Anchor points' locations (mm)	(x, y) = (±450, ±125)

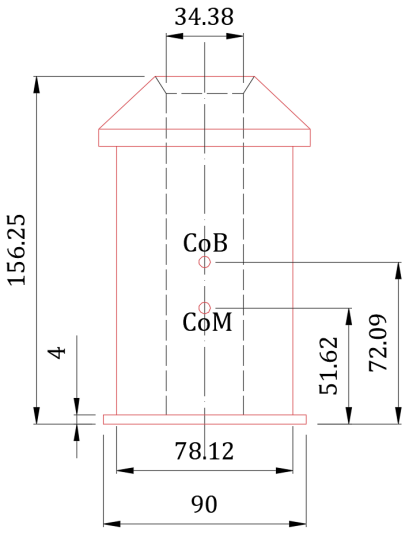

Fig. 4. Sketch of the MoonWEC prototype used in the study showing the positions of the centre of mass (CoM) and centre of buoyancy (CoB) (all dimensions are in mm).

3.3 Data acquisition

The system to acquire the free surface and reconstruct the incident and reflected waves (Zelt and Skjelbreia, 1992) during the tests at a sampling frequency of 1 kHz consisted of seven resistive-type wave gauges (shown in blue in **Fig. 2**). These gauges were distributed along the channel, with one gauge in front of the wave maker to control the accuracy of the wave generation, three gauges in front of the MoonWEC to perform the wave-reflection analysis, and three behind the MoonWEC to perform the wave-transmission analysis.

In addition, a GoPro camera (shown in red in **Fig. 2)** was installed outside the wave flume in front of the prototype to record its motion at 24 fps in full HD (1920 × 1024 pixels). The experiments were conducted in a dark environment with a controlled light source to enhance the contrast of the images. The procedure (Gaeta et al., 2020) to study the motion of floating objects, which is widely adopted in literature, was developed in a MATLAB environment. This procedure includes a calibration process to improve the quality and the final estimation of the object's motion by detecting control points on its surface. These control points for the MoonWEC prototype are shown as black squares on its floater in **Fig. 3**.

3.4 Experimental campaign

First, a free decay test, FD1 (**Table 3**), was conducted on the MoonWEC prototype. The prototype was manually lifted 25 mm upwards and released back into the water, i.e., released from a given excitation in heave. The device began to oscillate according to its natural frequency. Although an initial excitation in pitch was not provided, it was not completely zero, and therefore the device also rotated in pitch. This allowed us to measure the natural periods of the prototype both in heave and pitch.

Table 3. *Free decay test, used in the experiments and also to validate the CFD model with the given initial excitation in heave and pitch.*

Test	Heave Excitation (mm)	Pitch Excitation (mm)
FD1	25	~ 0

Second, a set of regular waves, as reported in **Table 4**, following the wave profile defined by Stokes 5th-order wave theory, was generated in the wave flume. The MoonWEC prototype was initially at rest in its equilibrium position and began to oscillate in response to the generated waves. The values of the wave heights (H) and wave periods (T) in **Table 4** were measured by wave gauge 4 (the fourth wave gauge from the left in **Fig. 2**), which is 710 mm away from the MoonWEC prototype.

Table 4. *Set of regular waves used in the experiments and also to validate the CFD model with wave heights and wave periods measured from wave gauge 4.*

Test	H	T

	(mm)	(s)
R01	11.24	0.63
R02	11.64	0.72
R03	16.26	0.82
R04	21.16	0.85
R05	25.28	0.94
R06	32.63	0.94

Because the experimental tests were conducted in a wave flume, the multi-directionality of the MoonWEC's response to waves could not be investigated for two main reasons. First, the videography system only allowed the MoonWEC's motion to be estimated in the x-z plane from the acquired planar images. Second, the boundary effects of the flume walls could not be assumed completely negligible.

3.4.1 Free decay test

Fig. 5 shows the heave (left) and pitch (right) response time series, and **Fig. 6** shows the heave (left) and pitch (right) response spectra for the free decay test (FD1). The spectra are generated by applying the Fast Fourier Transform (FFT) in MATLAB to the complete time series. After analysing the data, the natural periods of the MoonWEC prototype in heave and pitch were determined to be 0.77 s and 0.93 s respectively, as reported in **Table 5.**

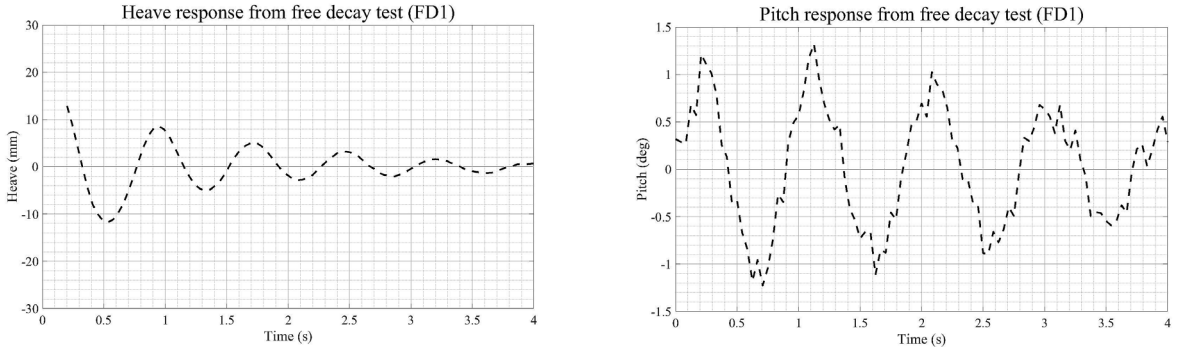

Fig. 5. MoonWEC's heave and pitch response time series for the free decay test (FD1) from the experiment.

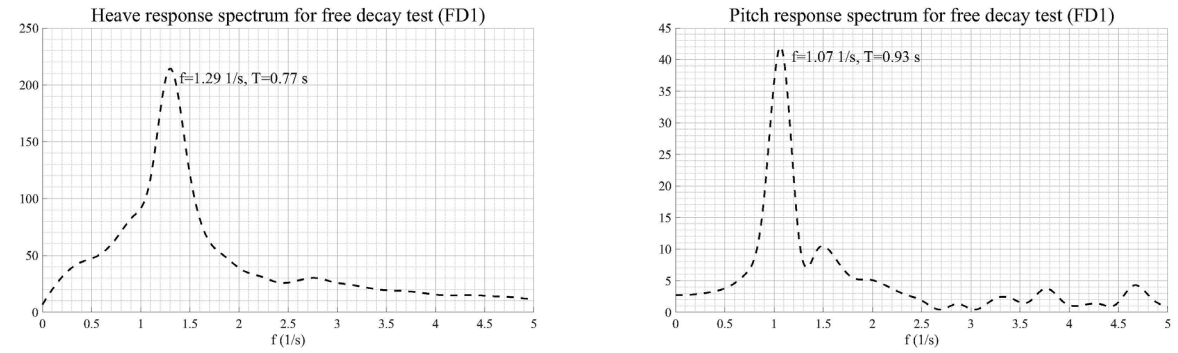

Fig. 6. MoonWEC heave and pitch response spectra from the free decay test (FD1) from the experiment.

Table 5. *Natural periods of the MoonWEC prototype in heave and pitch from free decay test (FD1) from the experiment.*

Parameter	FD1
$T_{n-heave}$ (s)	0.77
$T_{n-pitch}$ (s)	0.93

3.4.2 Wave-structure interaction tests

Fig. 7 shows the time series of MoonWEC heave amplitudes and wave amplitudes from the WSI tests (R01-R06). Using the values of these amplitudes, we can calculate the Response Amplitude Operator (RAO) following Equation (3), as the ratio between the maximum amplitude of the floating body motion, i.e., the maximum heaving amplitude (AM_{max}) of the

MoonWEC prototype, and the amplitude (A) of the wave causing that motion. During the experiments, the higher harmonics were not evident in the time series. Whereas the time series were smoothed using a highpass filter in MATLAB.

$$RAO = \frac{The\ maximum\ amplitude\ of\ floating\ body\ motion}{The\ amplitude\ of\ the\ wave\ causing\ that\ motion} = \frac{AM_{max}}{A} \quad (3)$$

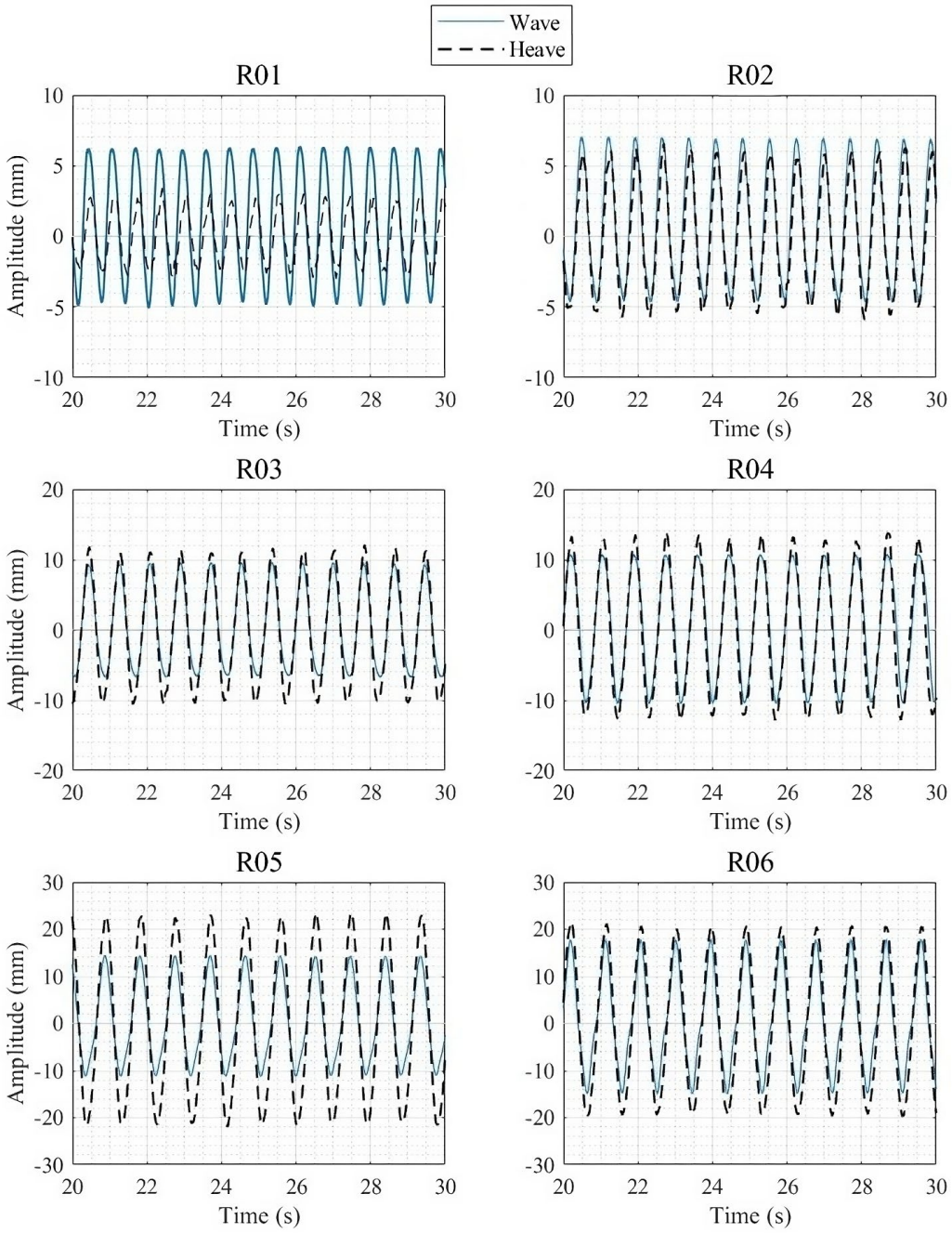

Fig. 7. MoonWEC heave and wave amplitudes for the WSI tests (R01-R06) from experiments.

The RAO values calculated for the six WSI tests are reported in **Table 6**. RAO values greater than 1 indicate that the device is excited more than the exciting wave, which is a positive outcome for energy conversion motion. In other words, if the device is well-tuned, it can oscillate with large amplitudes for even short amplitude waves, facilitating the energy conversion motion in heave.

Table 6. *RAO values in heave for the MoonWEC prototype calculated from experiments (R01-R06).*

Wave	T	A	AM_{max}	RAO

	(s)	(mm)	(mm)	(-)
R01	0.630	5.693	3.231	0.567
R02	0.720	5.854	6.156	1.052
R03	0.820	8.164	11.514	1.410
R04	0.850	10.614	13.373	1.260
R05	0.940	12.734	23.243	1.825
R06	0.940	16.361	21.054	1.287

4. Numerical simulations

A 3D NWT was created using OpenFOAM to analyse and optimize the hydrodynamic response of the small-scale MoonWEC prototype, used in the laboratory experiments. The CFD modelling of MoonWEC involved two fluid phases: water and air. The *overInterDyMFoam* solver was utilized for the multiphase simulation, which considers the 3D *Reynolds Averaged Navier-Stokes (RANS)* equations for two incompressible fluid phases using a Volume of Fluid (VoF) (Hirt and Nicholas, 1981) interface capturing approach based on phase fraction. The overset framework was used to simulate the interaction of the solid body with the fluid. The dynamic mooring library MooDy (Palm et al., 2017; Palm, 2017; Palm and Eskilsson, 2018) was used for computing the mooring cable dynamics, implemented as a hp-adaptive cable solver based on the discontinuous Galerkin method.

4.1 Governing equations for two-phase flow

The fluid motion of a moored floating body is governed by the Navier-Stokes (NS) equations. However, the numerical solver models the unsteadiness of the turbulence in the Reynolds Averaged Navier-Stokes (RANS) equations. The RANS equations include equations of continuity and mass conservation (Equations (4) and (5)), which are the governing mathematical expressions that link pressure and velocity. The assumption of incompressible fluids has been widely accepted in coastal engineering, as it applies to most practical problems (Higuera et al., 2013).

$$\nabla \cdot U = 0 \tag{4}$$

And,

$$\frac{\partial \rho U}{\partial t} + \nabla \cdot (\rho U U) - \nabla \cdot \left(\mu_{eff} \nabla U\right) = -\nabla p^* - g \cdot X \nabla \rho + \nabla U \cdot \nabla \mu_{eff} + \sigma \kappa \nabla \alpha \tag{5}$$

The elements in Equation (5) are arranged in a specific way, with those on the left-hand side being used in OpenFOAM to assemble the coefficient matrix and those on the right-hand side being calculated explicitly and forming the independent term of the equations.

α (-) is the volume fraction (VoF indicator phase function), defined as the quantity of a fluid per unit volume in each cell. It is assumed to be 1 for the water phase and 0 for the air phase.

U (m/s) is the velocity vector and is computed as,

$$U = \alpha_1 U_1 + \alpha_2 U_2 \tag{6}$$

Where α_1 and α_2 are the indicator phase functions of fluid 1 and fluid 2, respectively. In the current CFD model, we assume that α_1 represents the seawater fraction and α_2 represents the air fraction. If $\alpha_1 = 1$, the cell is full of seawater; if $\alpha_1 = 0$, the cell is full of air; and for every other case, it represents the interface between the two fluids. Calculating any of the fluid's properties at each cell is straightforward, by simply weighing them by the VoF function, as shown in the above velocity Equation (6).

ρ (kg/m^3) is the fluid density, and is calculated as a weighted average of the densities of fluid 1 and fluid 2, ρ_1 and ρ_2, respectively, using the volume fraction functions, α_1 and α_2, as weights:

$$\rho = \alpha_1 \rho_1 + \alpha_2 \rho_2 \tag{7}$$

p^* (Pa) is the pseudo-dynamic pressure,

g (m/s^2) is the acceleration due to gravity,

X (m) is the position vector as (x, y, z),

μ_{eff} (Pa·s) is the effective dynamic viscosity, which considers the molecular dynamic viscosity and the turbulent effects as,

$$\mu_{eff} = \mu + \mu_{turb} \tag{8}$$

Where,

$$\mu = \alpha_1\mu_1 + \alpha_2\mu_2 \tag{9}$$

And,

$$\mu_{turb} = \alpha_1\mu_{turb1} + \alpha_2\mu_{turb2} \tag{10}$$

μ_1 and μ_2 are the dynamic viscosities of fluid 1 and fluid 2, respectively, and μ_{turb1} and μ_{turb2} are the turbulent viscosities of fluid 1 and fluid 2, respectively, depending on the chosen turbulence model.

The last term on the right-hand side of Equation (5) represents the surface tension effect, where,

σ (N/m) is the coefficient of surface tension,

κ (1/m) is the interface curvature, which is calculated as follows:

$$\kappa = \nabla \cdot \frac{\nabla\alpha_1}{|\nabla\alpha_1|} \tag{11}$$

The classic advection equation is the starting point for the equation which tracks the fluid movement, as shown below:

$$\frac{\partial\alpha_1}{\partial t} + \nabla \cdot \alpha_1 U = 0 \tag{12}$$

However, there are some restrictions on achieving physically accurate results. OpenFOAM uses an artificial compression term, $\nabla\cdot(\alpha_1\alpha_2 U_r)$ (Weller, 2002), rather than a compressing differencing scheme, which leads to the following final expression for the phase continuity equation:

$$\frac{\partial\alpha_1}{\partial t} + \nabla \cdot \alpha_1 U + \nabla \cdot (\alpha_1\alpha_2 U_r) = 0 \tag{13}$$

Where U_r is the relative velocity vector between the two phases, computed as follows:

$$U_r = U_1 - U_2 \tag{14}$$

4.2 Numerical model setup

As stated by Windt et al. (2019), the costs of experiments in NWTs and physical wave tanks (PWTs) are highly case-dependent. However, NWTs have seen a large increase in application in recent years due to the ever-increasing availability of cheap computational power, while offering access to all field variables and flexibility in tank layout and experimental design. Additionally, compared to lower fidelity numerical tools, high-fidelity numerical models, such as CFD-based NWTs (CNWTs), have the advantage of capturing relevant hydrodynamic non-linearities, such as complex free surface elevation (including wave breaking), viscous drag and turbulence effects.

To reduce the computational cost in this study, the NWT was created to represent only a portion of the laboratory wave flume, while maintaining a length of at least two wavelengths. The exact dimensions of the NWT used for the simulations of the free decay and WSI tests are reported in **Table 9** and **Table 13**, respectively. The CFD model of the MoonWEC was reproduced using the overset mesh methodology. The methodology is described in (Romano et al., 2020). It is based on the use of two domains: a background domain and a moving domain. The background domain, which represents a portion of the wave flume, allows for the motion of the moving domain that contained MoonWEC. Overlapping the two domains creates a new mesh that can represent complex geometries with large displacements while maintaining good mesh quality. The inverseDistance method was used as the overset interpolation method in OpenFOAM.

A sketch of the NWT, with background and overset meshes, is shown in **Fig. 8**. A summary of the boundary conditions is provided in **Table A.1** and the physical properties of the two fluids in **Table A.2** in Appendix A. The MoonWEC was placed at the centre of the NWT. Wave generation and active wave absorption (using shallow-water theory), based on the

IHFOAM (Higuera et al., 2013) toolbox, were defined at the inlet boundary (on the left). Active wave absorption was also defined at the outlet boundary (on the right). Boundary conditions were set to a solid wall with a no-slip condition for the flume bottom (ground) and the MoonWEC. A slip condition for the front and back walls was applied. The top boundary (atmosphere) was left as an open boundary imposing a total pressure condition, where air and water could freely flow out and only air could flow in. The water depth was kept constant at 0.4 m throughout the domain. The wave properties used for the simulations were based on the regular Stokes 5th-order waves listed in **Table 4**.

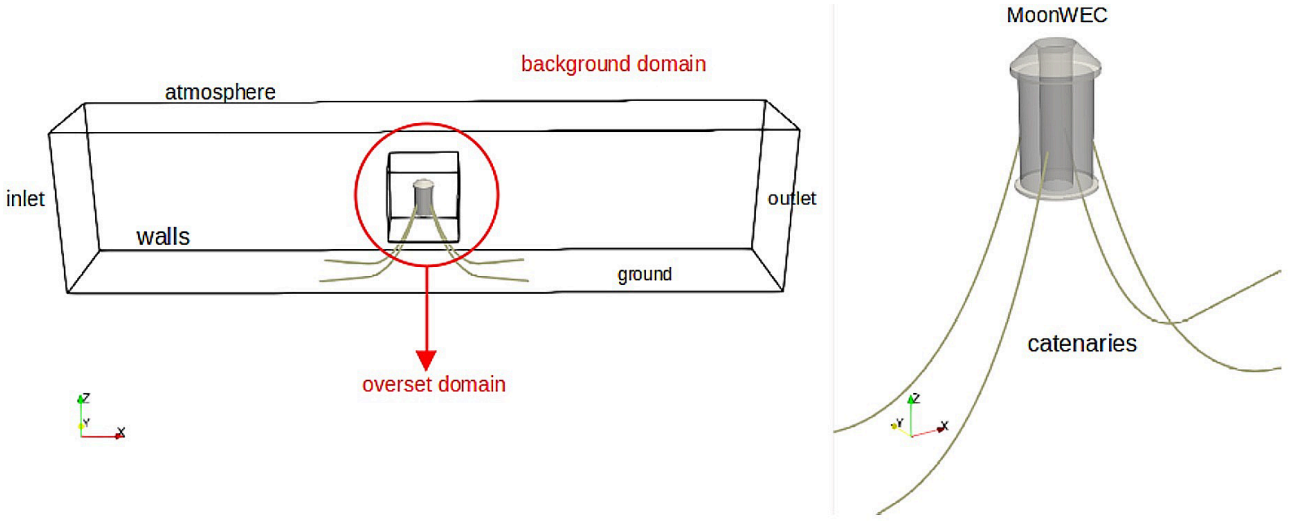

Fig. 8. NWT sketch indicating the boundary names and locations.

To ensure the proper behaviour of the MoonWEC prototype, i.e., to achieve the required draft and imitate its response from the experiments, its physical properties, calculated from its 3D CAD model in SolidWorks®, are defined in the model. These properties, including mass, centre of mass (CoM), and Moment of inertia, are provided in **Table 7**. The z-coordinate of the centre of mass, CoM_z, is 51.62 mm as also mentioned in **Table 2** and shown in **Fig. 4**.

Table 7. *Summary of physical properties of MoonWEC prototype.*

Parameter	Value
Mass (kg)	0.527
Centre of mass (CoM) (m)	(x, y, z) = (0.00, 0.00, 0.05162)
Moment of inertia (kg.m^2)	(I_x, I_y, I_z) = (0.00158315258, 0.00158315258, 0.00053606253)

When floating devices interact with waves, there are chaotic turbulent processes that dissipate kinetic energy and change fluid properties. These processes need to be modelled to simulate mean flow characteristics.

Several turbulence models can be applied to ocean engineering applications, such as the kEpsilon (k−ε) model (Di Paolo et al., 2018), the renormalization group kEpsilon (RNG−k−ε) model (Palm et al., 2016; Eskilson et al., 2017), the kOmega (k−ω) model (Xu and Huang, 2019), the kOmega shear stress transport (k−ω−SST) model (Iturrioz et al., 2015; Vukčević, 2016; Wang and Zhang, 2021; Katsidoniotaki and Göteman, 2022), and the Reynolds stress-omega (RS−ω) model (Li and Fuhrman, 2022), which is more complex and time-consuming to solve.

This study used the k−ω−SST turbulence model with the Larsen and Fuhrman (2018) enhancement to limit the overproduction of turbulence beneath surface waves. Wall functions were used to model the near-wall regions. For a description, validation, and discussion of the stabilized turbulence models, please refer to Larsen and Fuhrman (2018).

It was not the aim of this work to model and resolve the boundary layer around the MoonWEC. The inclusion of a detailed turbulence analysis caused by wave breaking or splashing near the floating device will be investigated in future works.

4.3 Mooring

To simulate the mooring chains, the dynamic mooring library MooDy was used. It was integrated with OpenFOAM version 2106. The cable parameters were defined in the model, including the number of cables, cable diameter, mass per unit length, attachment points on the MoonWEC's floater, and the anchor points on the ground. These parameters, provided in **Table 8**, corresponded to the mooring conditions used in the experiments. The z-coordinates of the anchor points were located on the flume bottom at a water depth of 400 mm, with a zero value indicating the origin at the flume bottom.

The attachment points on the MoonWEC prototype were located at a height corresponding to its centre of mass and along the circumference, 90° from each other. Given a water depth of 400 mm, a draft of 135 mm (reported in **Table 2**), and the z-coordinate of the centre of mass, CoM_z, of 51.62 mm, the z-coordinate of the attachment points on MoonWEC was 316.62 mm for WSI tests.

Table 8. *Summary of cable parameters as defined in the CFD model.*

Parameter	Value
Number of cables (no.)	4
Cable diameter (mm)	1.40
Cable length (mm)	620.00
Mass per unit length (g/m)	11.50
Anchor Point 1 (mm)	(x, y, z) = (-450, -125, 0)
Anchor Point 2 (mm)	(x, y, z) = (-450, 125, 0)
Anchor Point 3 (mm)	(x, y, z) = (450, -125, 0)
Anchor Point 4 (mm)	(x, y, z) = (450, 125, 0)
Attachment Point 1 on MoonWEC (mm)	(x, y, z) = (-0.0275772, -0.0275772, 316.62)
Attachment Point 2 on MoonWEC (mm)	(x, y, z) = (-0.0275772, 0.0275772, 316.62)
Attachment Point 3 on MoonWEC (mm)	(x, y, z) = (0.0275772, -0.0275772, 316.62)
Attachment Point 4 on MoonWEC (mm)	(x, y, z) = (0.0275772, 0.0275772, 316.62)

5. Validation against experimental data

This section presents an analysis of the numerical results and compares them with the experimental data. The original laboratory experiments were used as a reference for the validation of the NWT, which includes a free decay test (FD1) and six WSI tests (R01-R06). Two mesh convergence analyses were performed to define the optimal value of the mesh size for the simulations for the most representative benchmarks, FD1 and R06. These benchmarks were selected to analyse different types of displacements of the MoonWEC prototype caused by different triggering conditions. Qualitative and quantitative comparisons of heave and pitch motions are presented.

5.1 Free decay test

The response of the MoonWEC to a heave excitation was numerically reproduced and compared with experimental data. To achieve this, similar initial conditions to those of the FD1 experiment were replicated in the CFD model, i.e., the MoonWEC prototype was released from an initial heave excitation of +25 mm with no excitation in pitch, as reported in **Table 3**.

5.1.1 Grid analysis for FD1

In this study, we chose not to add any refinement around the free surface to minimize instabilities caused by the interaction of the structure with the incoming waves. Large displacements of complex structures and breaking waves simulated under extreme weather conditions in the overset framework with a refinement around the structure can lead to instabilities that may produce unrealistic results.

To determine the optimal mesh for the free decay test, we used the maximum heave in the decay test (FD1) as a unique measure for each grid size. Three different discretization levels were examined: a coarse-mesh with 3 cells per maximum heave (CMH), Mesh 1; a medium-mesh with 5 CMH, Mesh 2; and a fine-mesh with 7 CMH, Mesh 3. The characteristics of these meshes are summarized in **Table 9,** which shows the mesh dimensions for the background and the overset meshes and the corresponding discretization. In the overset domain, a mesh refinement with a cell size of ¼ of the discretization is defined around the MoonWEC.

Table 9. CFD meshes for the free decay test FD1.

Mesh	Overset		Background		Total Number of Cells (no.)
	Numerical Domain x × y × z (mm × mm × mm)	Discretization dx × dy × dz (mm × mm × mm)	Numerical Domain x × y × z (mm × mm × mm)	Discretization dx × dy × dz (mm × mm × mm)	
Mesh 1	300 × 300 × 300	13.64 × 13.64 × 8.33	500 × 500 × 800	13.89 × 13.89 × 8.6	137,952
Mesh 2	300 × 300 × 300	10.71 × 10.71 × 6.67	500 × 500 × 800	10.87 × 10.87 × 6.9	280,736

Mesh 3	300 × 300 × 300	8.82 × 8.82 × 5.45	500 × 500 × 800	8.62 × 8.62 × 5.52	551,360

Katsidoniotaki and Göteman (2022) state that the spatial and temporal discretization is connected through the Courant-Friedrichs-Lewy (CFL) condition, which adjusts the variable time step.

The discrimination ratio, R_D, provides information about the convergence or divergence of the study. Based on the solutions for the finest (S_f, Mesh 3), medium (S_m, Mesh 2) and coarsest (S_c, Mesh 1) discretization sizes:

$$R_D = \frac{\varepsilon_{fm}}{\varepsilon_{mc}} = \frac{S_f - S_m}{S_m - S_c} \tag{15}$$

R_D is used to differentiate four types of convergence, as summarized in **Table 10.**

Table 10. Convergence or divergence criterion based on the discrimination ratio R_D.

Type	Convergence	Divergence
Monotonic	$0 < R_D < 1$	$R_D < 0$ and $\lvert R_D \rvert < 1$
Oscillatory	$R_D > 1$	$R_D < 0$ and $\lvert R_D \rvert > 1$

The absolute grid uncertainty, U_a, can be calculated for monotonic convergence:

$$U_a = F_s \frac{\varepsilon_{fm}}{r^p - 1} \tag{16}$$

where F_S is the safety factor (1.5), r is the refinement ratio and p is the order of accuracy:

$$p = \frac{ln(\frac{\varepsilon_{fm}}{\varepsilon_{mc}})}{ln(r)} \tag{17}$$

In the case of oscillatory convergence, the uncertainty is calculated following the method proposed by Stern et al. (2001):

$$U_a = F_s \times 0.5 \, |S_U - S_L| \tag{18}$$

where S_U and S_L are the maximum (upper) and minimum (lower) results, respectively, among all solutions (coarse (Mesh1), medium (Mesh 2) and fine (Mesh 3)).

According to **Table 11**, R_D proves monotonic convergence (R_D=0.304), with a resulting relative grid uncertainty of 0.517%, which indicates a satisfactory level of convergence. To balance numerical model accuracy and computational cost, the cell resolution from the medium-mesh (Mesh 2), with 5 CMH, was used to perform the simulations. These results are consistent with the work of Katsidoniotaki and Göteman (2022) and Pinguet et al. (2022).

Table 11. Relative discretization uncertainty, U_a, for the free decay test (FD1).

Parameter	Mesh 1	Mesh 2	Mesh 3	r (-)	U_a [%]
Maximum Heave (mm)	0.399	0.391	0.388	1.25	0.517

Fig. 9 shows screenshots of the vertical velocity, U_z (m/s), represented only on the water (0.5 < VoF < 1.0) for the maximum heave displacement achieved for the three meshes (3 CMH, 5 CMH and 7 CMH). All three meshes reproduce the same hydrodynamic patterns around the structure. Furthermore, the medium and fine meshes reproduce vertical velocities with the same order of magnitude at the bottom of the structure.

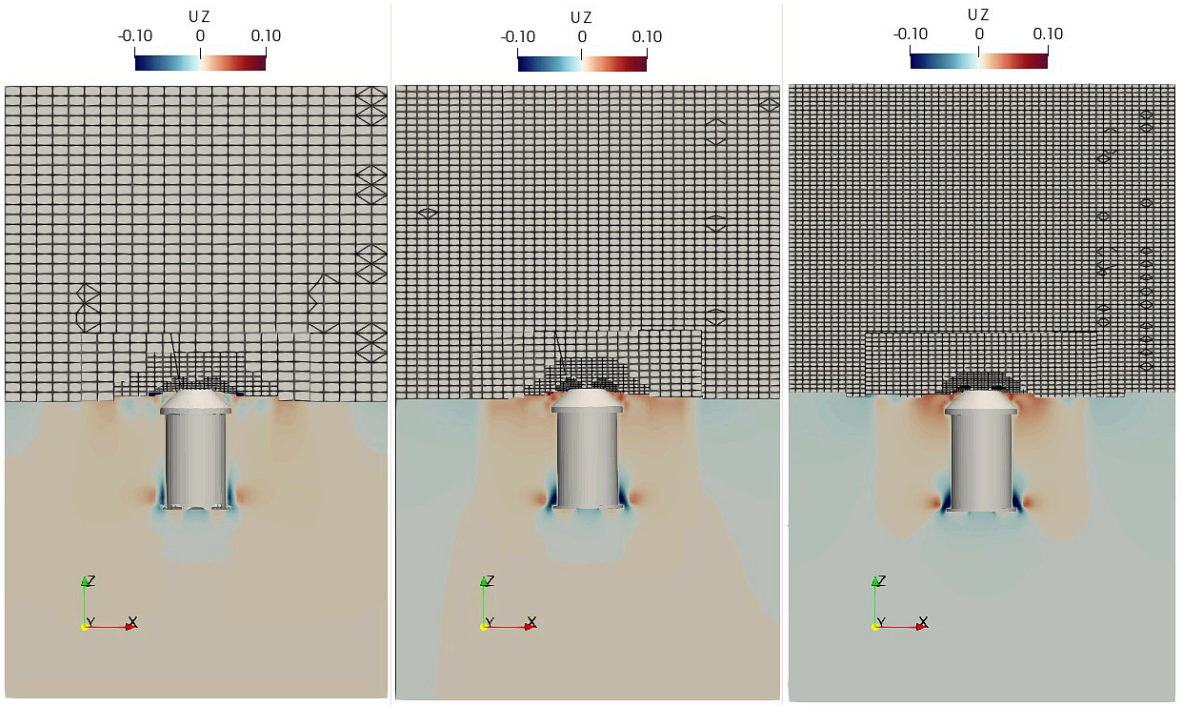

Fig. 9. Examples of different meshes using different cell sizes. Left panel Mesh 1 with 3 CMH, middle panel Mesh 2 with 5 CMH, right panel Mesh 3 with 7 CMH. Free decay test (FD1), at the moment of maximum heave displacement. Vertical velocity, U_z (m/s), displayed only in the water (0.5 < VoF < 1.0). Cell size is displayed in the background. (catenaries are not visible)

5.1.2 Validation of the CFD model against experiment FD1

To qualitatively assess the accuracy of the CFD model, we have compared the GoPro videos from the laboratory experiments with the 3D animation from the OpenFOAM case. **Fig. 10** shows a qualitative comparison between the CFD model (left) and the experiments (right), demonstrating the position of the prototype captured from both methods at different timesteps for the free decay test (FD1). By observing both images side by side, we can conclude that the CFD model has reproduced the prototype's behaviour very well.

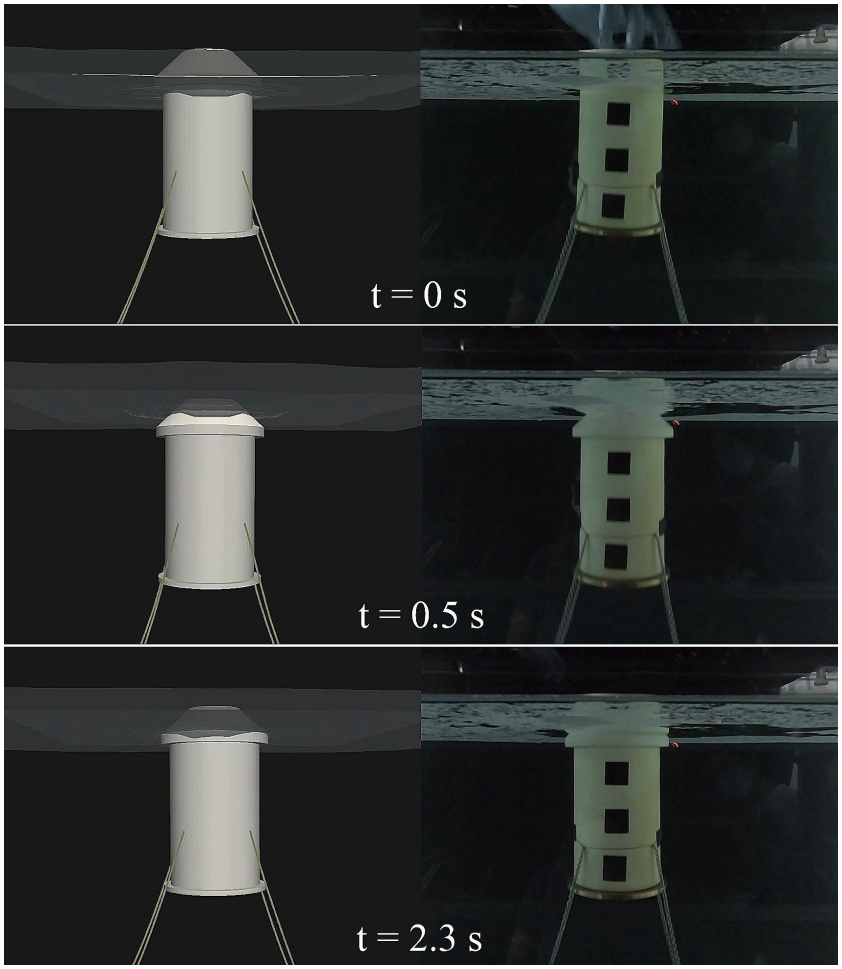

Fig. 10. MoonWEC CFD simulation (left) vs. laboratory experiments (right) for the free decay test (FD1) at different time steps.

To quantitatively assess the accuracy of the CFD model, the experimental data obtained from experiment FD1 is compared with the numerical simulation (Mesh 2). The heave and pitch response time series of the prototype, for FD1, are depicted in **Fig. 11**, comparing the numerical model and the experiments. It can be observed that the heaving amplitudes of the MoonWEC prototype from the FD1 are very similar for the numerical model and experiments. However, the amplitudes of the pitch response are larger in the experiments, likely due to handling errors as the device was released manually and some initial pitch excitation was present. In the CFD model, even though there is pitch in the heave decay test, it is very small (± 0.5 °), which could be due to the immersion and gentle splash caused by the device when it displaces the water. This is understandable, as the pitch rotation was not restricted in the OpenFOAM code. The same trend can be seen in **Fig. 12**, for the response spectra, which show similar peaks for the heave response between the numerical model and the experiments, while a slightly higher peak for the pitch response in the experiments. Apart from this difference, the free decay test from the numerical model provides the same natural periods of the device as measured in laboratory experiments.

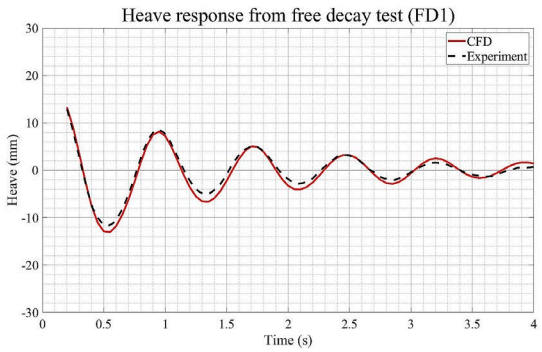

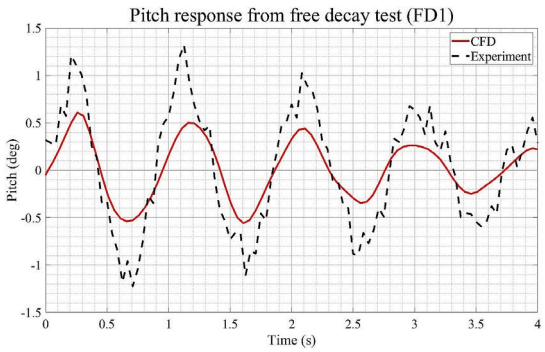

Fig. 11. MoonWEC's heave (left) and pitch (right) response time series for the free decay test (FD1) from the CFD model and experiment considering Mesh 2 with 5 CMH.

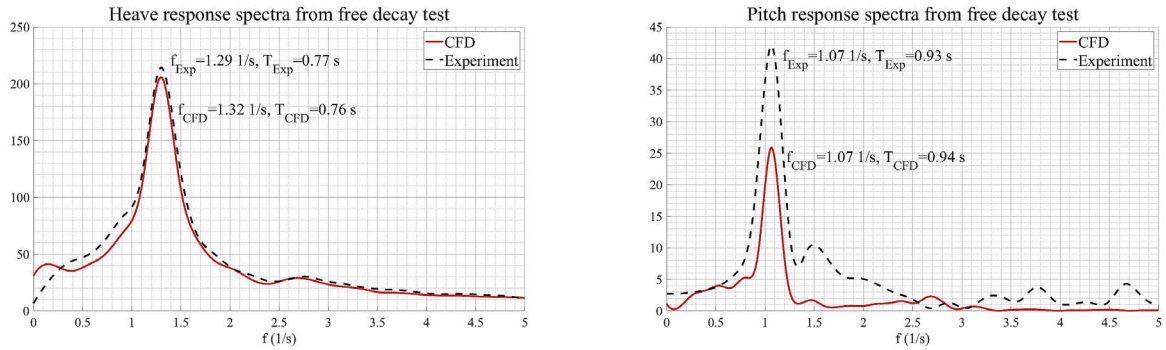

Fig. 12. MoonWEC's heave (left) and pitch (right) response spectra for the free decay test (FD1) from the CFD model and experiment considering Mesh 2 with 5 CMH.

Table 12 shows the values of the natural periods of the MoonWEC prototype in heave and pitch for the numerical simulation and the experiments. The natural periods of the device from the numerical model correspond to the actual natural periods of the device from the experiments, both in heave and pitch. The differences, shown in **Table 12**, are calculated using Equation (19), where T_{Exp} is the period calculated from the experiments and T_{CFD} is the period calculated from the CFD model. Differences of 1.29% and 1.08% are observed for the natural periods in heave and pitch, respectively.

$$Difference = \frac{T_{Exp} - T_{CFD}}{T_{Exp}} \times 100 \quad (19)$$

Table 12. Natural periods of the MoonWEC prototype in heave and pitch from the CFD model and the experiment considering Mesh 2 with 5 CMH.

	$T_{n-heave}$	$T_{n-pitch}$
Experiment (s)	0.77	0.93
CFD (s)	0.76	0.94
Difference (%)	1.29	1.08

5.2 Wave-structure interaction tests

WSI tests from experiments R01-R06 were reproduced using the CFD model to cross-validate the behaviour of the prototype in heave. The MoonWEC prototype was initially at rest floating at its equilibrium position and started to oscillate as the waves were generated. The experiments used for this validation correspond to the ones mentioned in **Table 4**.

5.2.1 Grid analysis for R06

To determine the optimum mesh for the WSI test, the maximum heave in the R06 WSI test (4 periods) from the experimental data was chosen as a unique measure for each grid size. Three different discretization levels were examined: a coarse-mesh with 4 cells per wave height (CPH), Mesh 1; a medium-mesh with 6 CPH, Mesh 2; and a fine-mesh with 9 CPH, Mesh 3. The characteristics of these meshes are summarized in **Table 13**. In the overset domain, a mesh refinement with a cell size of ¼ of the discretization is defined around the MoonWEC.

Table 13. CFD meshes for the WSI test (R06).

	Overset		Background		
Mesh	Numerical Domain x × y × z (mm × mm × mm)	Discretization dx × dy × dz (mm × mm × mm)	Numerical Domain x × y × z (mm × mm × mm)	Discretization dx × dy × dz (mm × mm × mm)	Total Number of Cells (no.)

Mesh 1	300 × 300 × 300	13.64 × 13.64 × 8.33	3000 × 500 × 700	13.7 × 13.16 × 8.43	708,150
Mesh 2	300 × 300 × 300	9.38 × 9.38 × 5.88	3000 × 500 × 700	9.38 × 9.26 × 5.98	2,073,984
Mesh 3	300 × 300 × 300	6.52 × 6.52 × 3.95	3000 × 500 × 700	6.52 × 6.58 × 4	6,278,816

According to **Table 14**, R_D proves monotonic convergence (R_D=0.812), with a resulting relative grid uncertainty of 1.04%, which indicates a satisfactory level of convergence. To balance numerical model accuracy and computational cost, the cell resolution from the medium-mesh (Mesh 2), with 6 CPH was used to perform the simulations. These results are again consistent with the work of Katsidoniotaki and Göteman (2022) and Pinguet et al. (2022).

Table 14. Relative discretization uncertainty, U_a, for the WSI test (R06).

Parameter	Mesh 1	Mesh 2	Mesh 3	r (-)	U_a [%]
Wave Amplitude (mm)	0.032	0.031	0.029	1.45	1.04

Fig. 13 presents screenshots of the horizontal velocity, U_x (m/s), represented on the water only (0.5 < VoF < 1.0) for the three meshes (4 CPH, 6 CPH and 9 CPH). All three meshes reproduce the same hydrodynamic patterns around the structure, with the medium and fine mesh reproducing horizontal velocities of the same order of magnitude at the bottom of the structure.

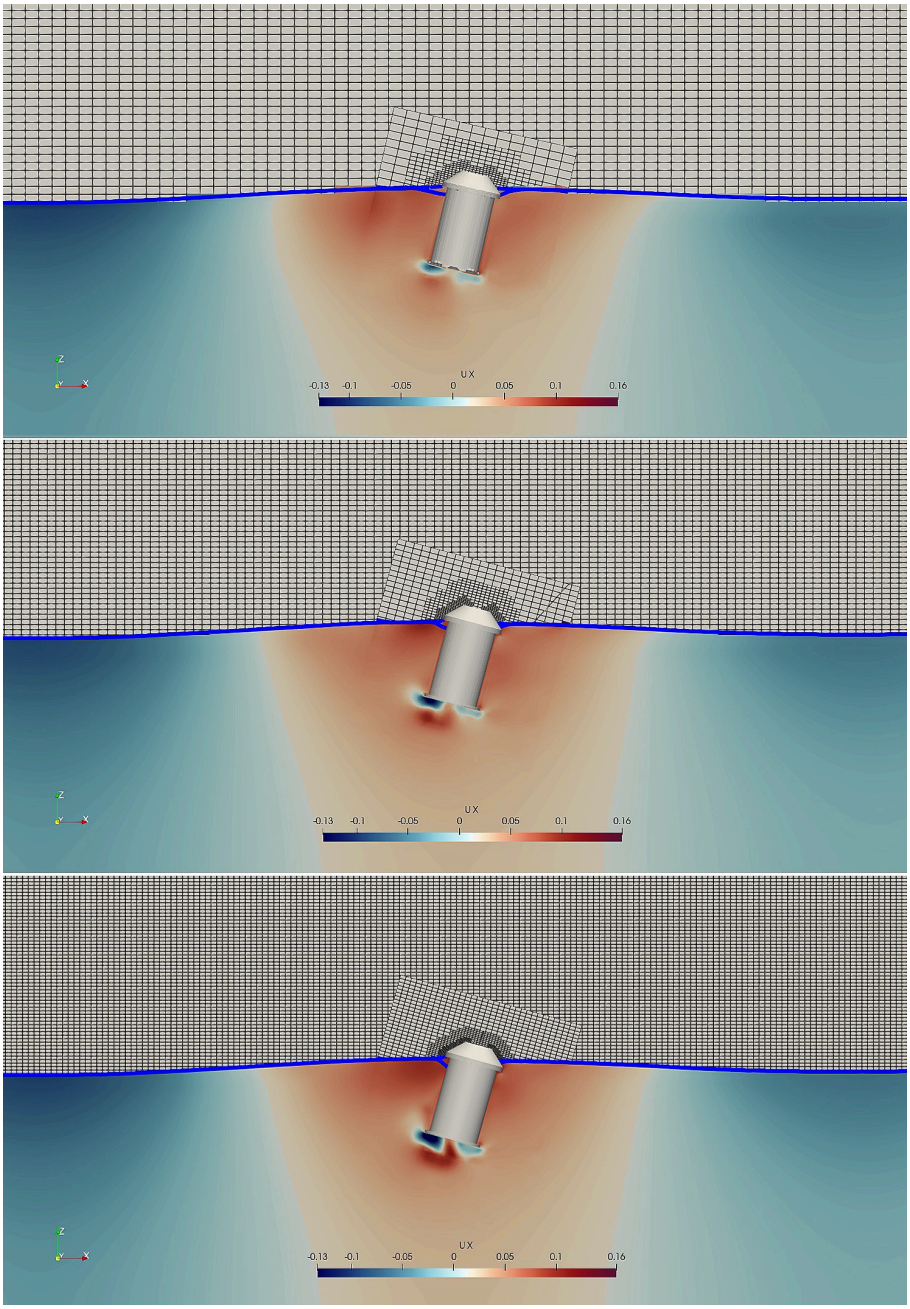

Fig. 13. Examples of different meshes using different cell sizes. Top panel Mesh 1 with 4 CPH, middle panel Mesh 2 with 6 CPH, bottom panel Mesh 3 with 9 CPH. Wave test R06. Horizontal velocity, U_x (m/s), displayed only in the water (0.5<VoF<1.0). Cell size is displayed in the background. (Catenaries are not visible)

5.2.2 Validation of the CFD model against experiments R01-R06

The accuracy of the CFD model is qualitatively demonstrated by comparing the GoPro videos from the laboratory experiments with the 3D animation from OpenFOAM in **Fig. 14** at different timesteps for the test case R06. Good agreement can be observed for the movement of the MoonWEC and the display of the catenaries.

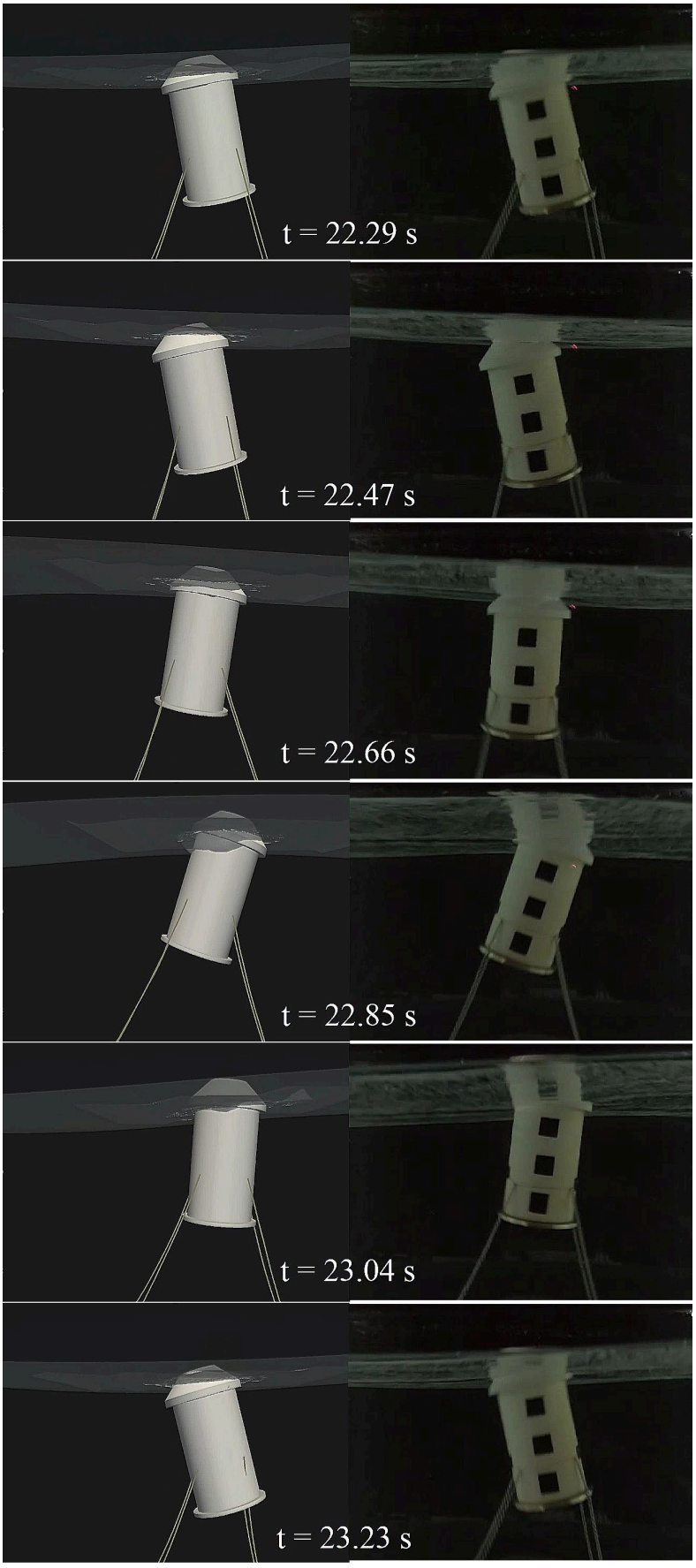

Fig. 14. MoonWEC CFD simulation (left) vs. laboratory experiments (right) for the WSI test (R06) at different time steps over a single wave period of T=0.94 s.

To quantitatively assess the accuracy of the NWT, the free surface elevations and heave motions from the six WSI experiments (R01-R06) are plotted against the numerical data in **Fig. 15**. **Table 15** summarizes the mean heaving amplitudes of the MoonWEC prototype obtained from the experiments and the CFD model, as well as the difference between the two values, calculated using Equation (19).

The CFD model is able to accurately reproduce the prototype's behaviour compared to the laboratory experiments, Larger differences are observed (12.54%, 10.81% and 6.66%) for the less energetic cases (R01, R02 and R03), and smaller differences (3.57%, 1.18% and 2.61%) for the more energetic ones (R04, R05, R06).

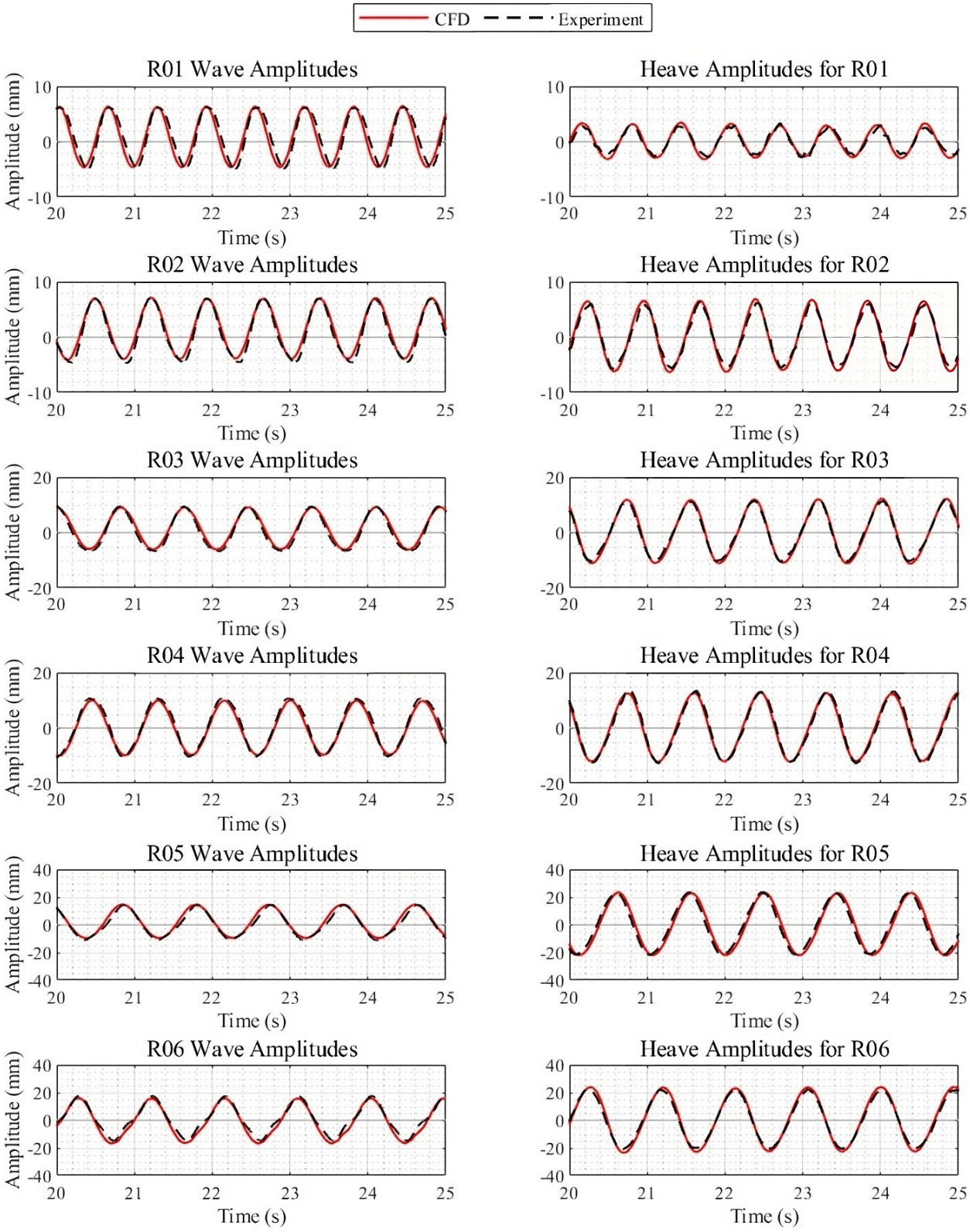

Fig. 15. Wave amplitudes (left) and MoonWEC heave response (right) for the WSI tests (R01-R06) from the CFD model and experiments considering Mesh 2 with 6 CPH.

Table 15. Mean MoonWEC heaving amplitudes for the WSI tests (R01-R06) from the CFD model and experiments considering Mesh 2 with 6 CPH.

	R01	R02	R03	R04	R05	R06
Experiment (mm)	5.49	11.467	21.86	25.84	44.92	42.32
CFD (mm)	6.18	12.71	23.32	24.92	45.45	43.43
Difference (%)	12.54	10.81	6.66	3.57	1.18	2.61

6. MoonWEC hydrodynamic response optimization

6.1 Minimizing the pitch motion

During the CFD simulations and experiments, the pitch motion was observed to be excessively high, hindering the piston-type vertical motion of the moonpool. Therefore, after validating the NWT against the physical experiments, we aimed to ameliorate the pitch response by varying the mass properties.

Two additional virtual prototypes are considered. The mass properties of the original prototype, henceforth called CoM_1, were defined in **Table 7**. **Table 16** summarizes the mass properties of the other two new numerical prototypes as well, namely CoM_2 and CoM_3. **Fig. 16** shows the sketches of the three prototypes with their centres of mass and centres of buoyancy, where the original prototype, CoM_1, is shown in red, CoM_2 is shown in green, and CoM_3 is shown in blue.

Table 16. *Summary of the mass properties of three MoonWEC virtual prototypes.*

Prototype	Parameter	Value
CoM_1	Mass (kg)	0.527
	Centre of mass (m)	(x, y, z) = (0.00, 0.00, 0.05162)
	Moment of inertia (kg.m^2)	(I_x, I_y, I_z) = (0.00158315258, 0.00158315258, 0.00053606253)
CoM_2	Mass (kg)	0.527
	Centre of mass (m)	(x, y, z) = (0.00, 0.00, 0.06700)
	Moment of inertia (kg.m^2)	(I_x, I_y, I_z) = (0.00145294857, 0.00145294857, 0.00051277255)
CoM_3	Mass (kg)	0.527
	Centre of mass (m)	(x, y, z) = (0.00, 0.00, 0.03600)
	Moment of inertia (kg.m^2)	(I_x, I_y, I_z) = (0.00146303954, 0.00146303954, 0.00146303954)

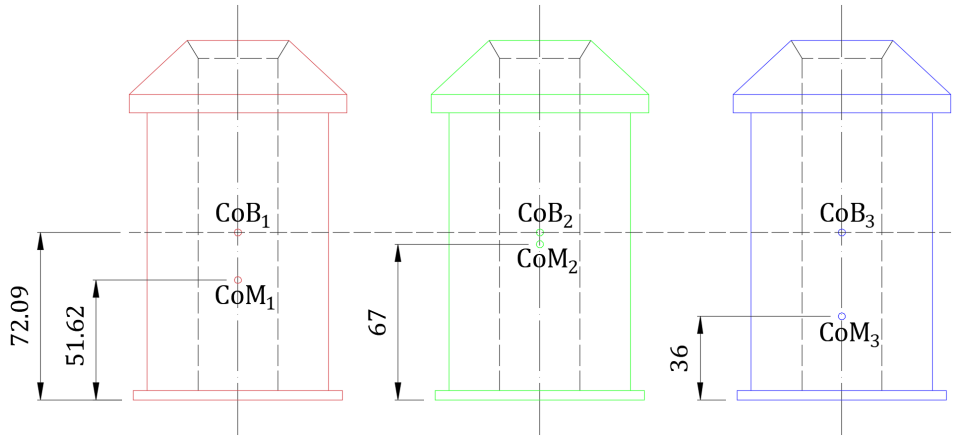

Fig. 16. Sketches of the three MoonWEC prototypes showing the positions of their centres of mass and centres of buoyancy (all dimensions are in mm).

For CoM_2, the centre of mass was shifted up towards the centre of buoyancy, from 51.62 mm to 67 mm. The centre of mass of 67 mm was chosen as an acceptable value for CoM_2, which is below the centre of buoyancy (CoB), to maintain stability. For CoM_3, the centre of mass was shifted down from 51.62 mm to 36 mm.

Shifting the centre of mass did not affect the heaving period of the device, as shown by the heave response time series in **Fig. 17** (left) and heave response spectra in **Fig. 18** (left) from the free decay test for the three CoMs. However, as shown in the pitch response time series in **Fig. 17** (right) and pitch response spectra in **Fig. 18** (right), the pitching period of the device changed significantly, from 0.94 s for CoM_1 to 1.6 s for CoM_2 and 0.75 s for CoM_3. Therefore, by modifying the device accordingly, the pitching period can be removed from the available range of the wave periods, so that the prototype cannot achieve resonance in pitch motion, thereby keeping the vertical motion of the device and the moonpool relatively undisturbed.

Fig. 19 compares the heave and pitch motion of the prototype against the 0.75 s wave for the three CoMs. The heave motion of all three prototypes is almost the same because they all have the same natural period in heave. However, the pitch motion for the same wave has been significantly changed. It is reduced by 3.5 times when the centre of mass is shifted upwards and amplified by 3 times when the centre of mass is shifted downwards. CoM_3, which has the same natural period in pitch of 0.75 s as the wave period, is the most amplified in pitch, while CoM_1 produces less pitch and CoM_2 the least, as expected, since they have pitch natural periods of 0.94 s and 1.6 s respectively (different from the wave period). A qualitative comparison of the maximum pitch positions in each direction (positive and negative) is shown in **Fig. 20** between CoM_1 and CoM_2. A significant reduction in the pitch for CoM_2 can be observed.

This ability to study the physical design of floating WECs accurately using CFD is a valuable asset, as it is very costly to study the hydrodynamics of the devices in real time by deploying them in the ocean or by using prototypes in laboratories.

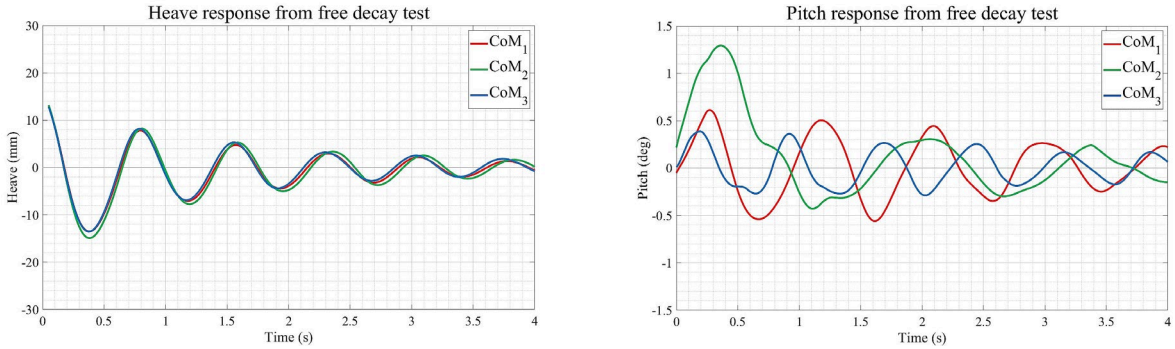

Fig. 17. MoonWEC's heave (left) and pitch (right) response time series from free decay test for 3 different CoMs.

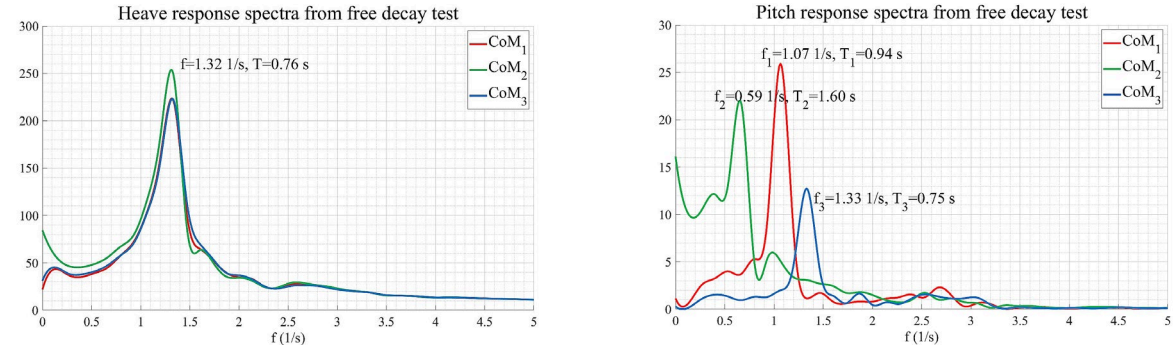

Fig. 18. MoonWEC's heave (left) and pitch (right) response spectra from free decay test for 3 different CoMs.

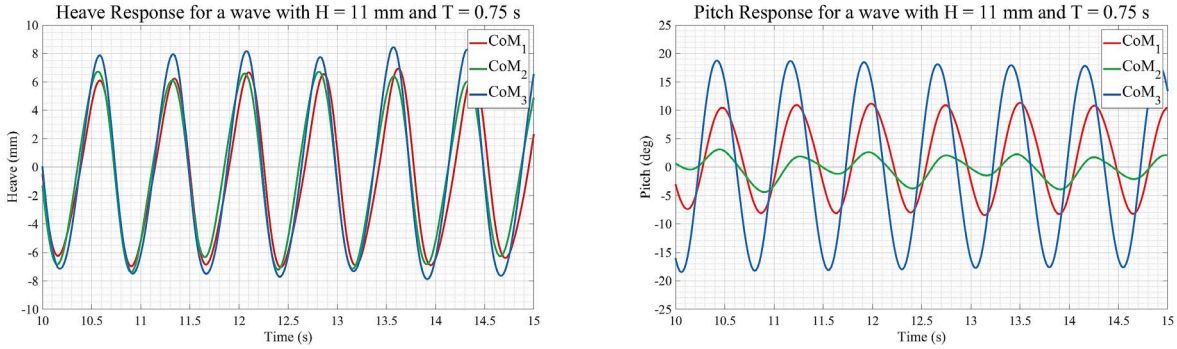

Fig. 19. MoonWEC's heave (left) and pitch (right) response time series from the WSI test for 3 different CoMs (H=11 mm and T=0.75 s).

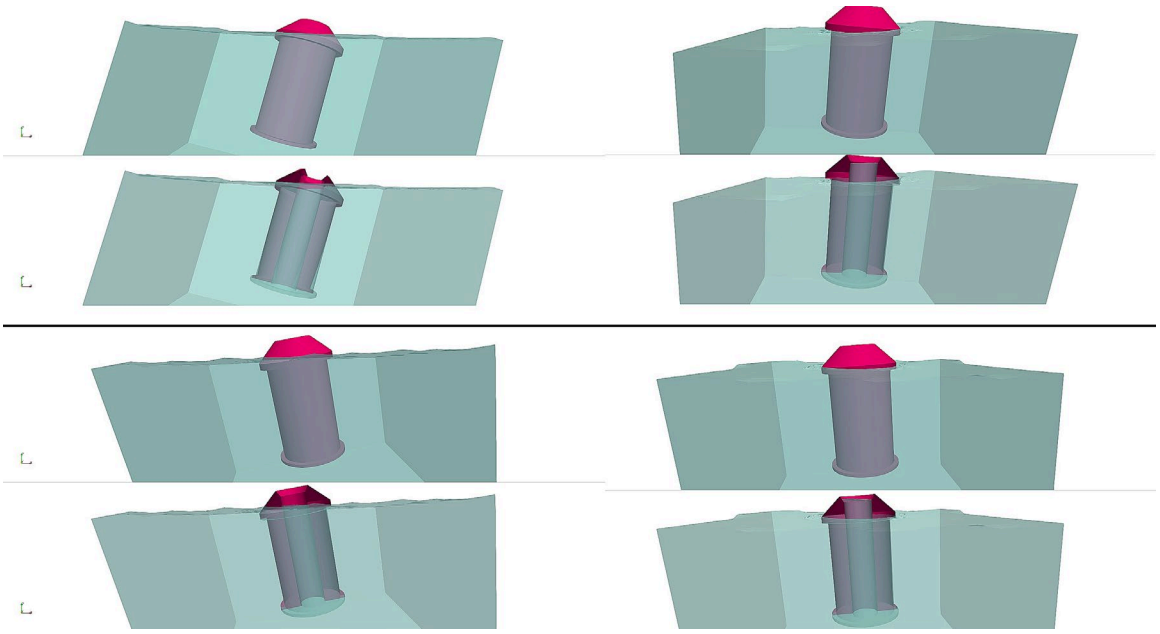

Fig. 20. CFD simulation at two maximum pitch positions in each direction for the CoM_1 (left) and CoM_2 (right) for the WSI test (H=11 mm and T=0.75 s).

6.2 Evaluating the optimized prototype for different wave periods

As demonstrated in section 6.1, CoM_2 performed better in reducing pitch for the given range of wave periods. Therefore, its response was studied further with a new set of regular waves, reported in **Table 17**, where H is the wave height and T is the wave period. **Fig. 21** (left) shows the heave amplitudes of CoM_2 in time. The device achieved the maximum heave excitation for the test case TW2, which coincides with the prototype CoM_2's natural heave period. The heave was also amplified for waves with a period higher than the device's natural period. The pitch rotations for the four test waves are shown in **Fig. 21** (right). The rotations tended to increase initially, especially for waves TW2 and TW3, but stabilized as the simulation proceeded. Nevertheless, the values remained sufficiently small (± 5 °).

Fig. 22 shows the heave (left) and pitch (right) response spectra. The peak with the maximum amplitude for the heave response is associated with TW2, while the test case TW1 has the lowest peak, corresponding to the wave period lower than the prototype's natural period. The pitch response has two higher peaks for the TW2 and TW3 test cases and lower peaks for the TW1 and TW4 test cases. However, the overall pitch response is sufficiently small that it does not hinder the energy conversion motion for the considered waves. The two higher peaks for TW2 and TW3 might be related to the fact that the wave periods for these two waves are almost half of the prototype's natural period in pitch, i.e., 1.6 s. The RAO values in heave, calculated using Equation (3) are shown in **Table 18**, where T is the wave period, A is the wave amplitude and AM_{max} is the maximum heaving amplitude of the MoonWEC prototype. These RAO values are also plotted in **Fig. 23**. The maximum heave RAO corresponds to the TW2 test case. The RAO values greater than 1 demonstrate the prototype's potential to achieve excitation in heave even for the waves that do not correspond to its natural period.

Table 17. *Set of regular waves used to study the hydrodynamic response of CoM_2.*

Test	H (mm)	T (s)
TW1	15	0.65
TW2	15	0.75
TW3	15	0.85
TW4	15	0.95

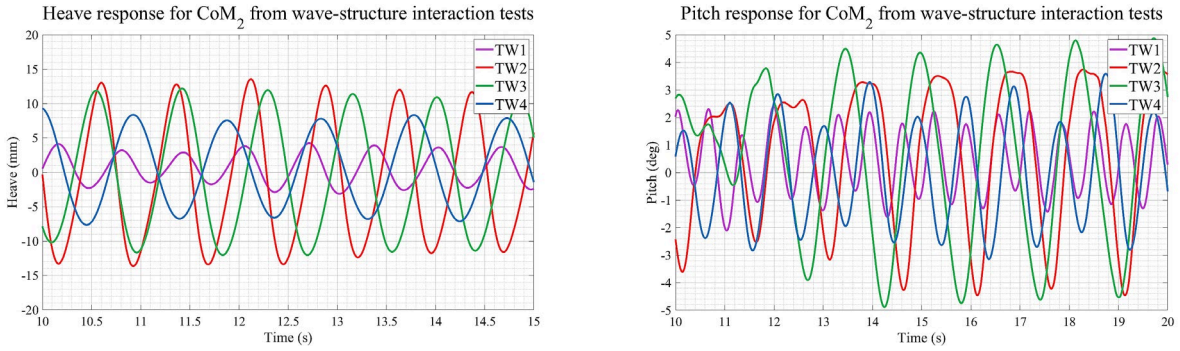

Fig. 21. CoM_2's heave (left) and pitch (right) response time series from the WSI test for four waves.

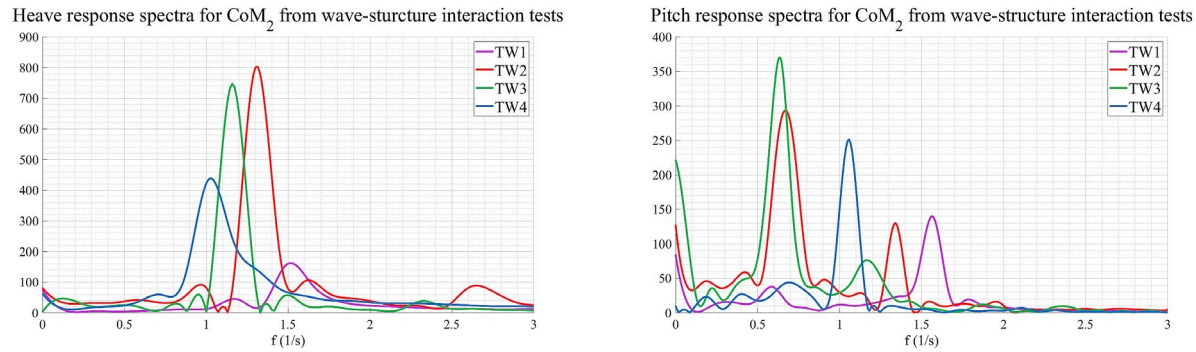

Fig. 22. CoM_2's heave (left) and pitch (right) response spectra from the WSI test for four waves.

Table 18. *Heave RAO values for the CoM_2 prototype.*

Test	T (s)	A (mm)	AM_{max} (mm)	RAO (-)
TW1	0.65	7.5	4.201	0.560
TW2	0.75	7.5	13.53	1.804
TW3	0.85	7.5	12.15	1.620
TW4	0.95	7.5	9.28	1.237

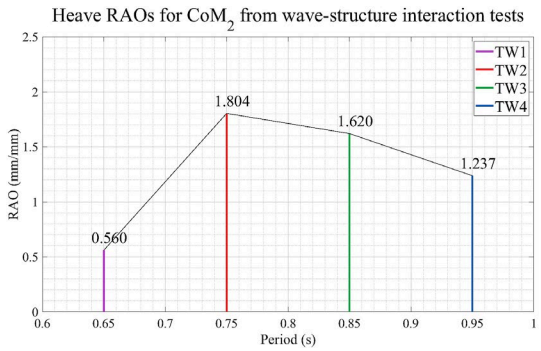

Fig. 23. Heave RAO for the CoM_2 prototype for four regular waves.

6.3. Evaluating the moonpool motion for an optimized prototype

The optimal configuration of the prototype is achieved with CoM_2, which reduces pitch and maximizes heave. The behaviour of CoM_2 can be further investigated by examining the moonpool dynamics, as the moonpool oscillations should also be amplified for optimal power production.

Following Equation (2), for the current configuration of the MoonWEC, the natural frequency of the moonpool with a draft of 0.135 m is 8.52 radians, corresponding to a natural period of 0.74 s, which is close to the natural period in heave of the MoonWEC prototype.

Fig. 24 shows the response of the MoonWEC prototypes, CoM_2 and CoM_3, in heave and pitch with the moonpool oscillations for test case TW2. Because the natural period in heave is unchanged, the heave response of both prototypes is almost the same. As expected, the pitch response is much higher for CoM_3. A trend can be observed for the moonpool oscillations: they are the maximum for CoM_2 with a ratio between the moonpool and wave amplitudes of 2.34. For CoM_3, the moonpool oscillations are higher initially and then start to decrease as the pitch motion of the MoonWEC tends to increase. Therefore, the higher pitch motion worsens the moonpool oscillations. Furthermore, the phase lag between the heave motion and the moonpool oscillations exists in both prototypes, but it is not completely opposite (180°). This might be due to the pitch rotations which in CoM_2 are significantly minimized but not completely eliminated. **Fig. 25** shows the CFD simulation for CoM_2 at different time steps for a duration of 1 period of the moonpool oscillation. The piston-type motion of the moonpool can be observed, going up and down at the centre of the MoonWEC.

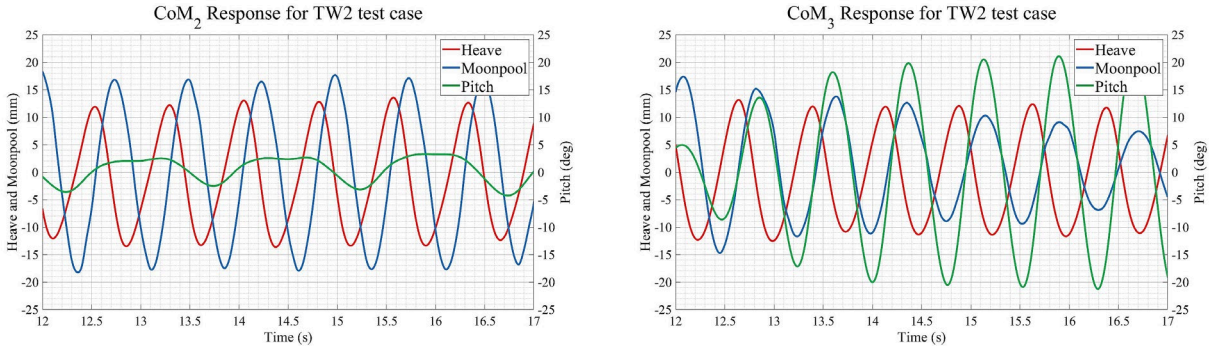

Fig. 24. CoM_2 and CoM_3 response in heave and pitch with moonpool oscillations for TW2 test case.

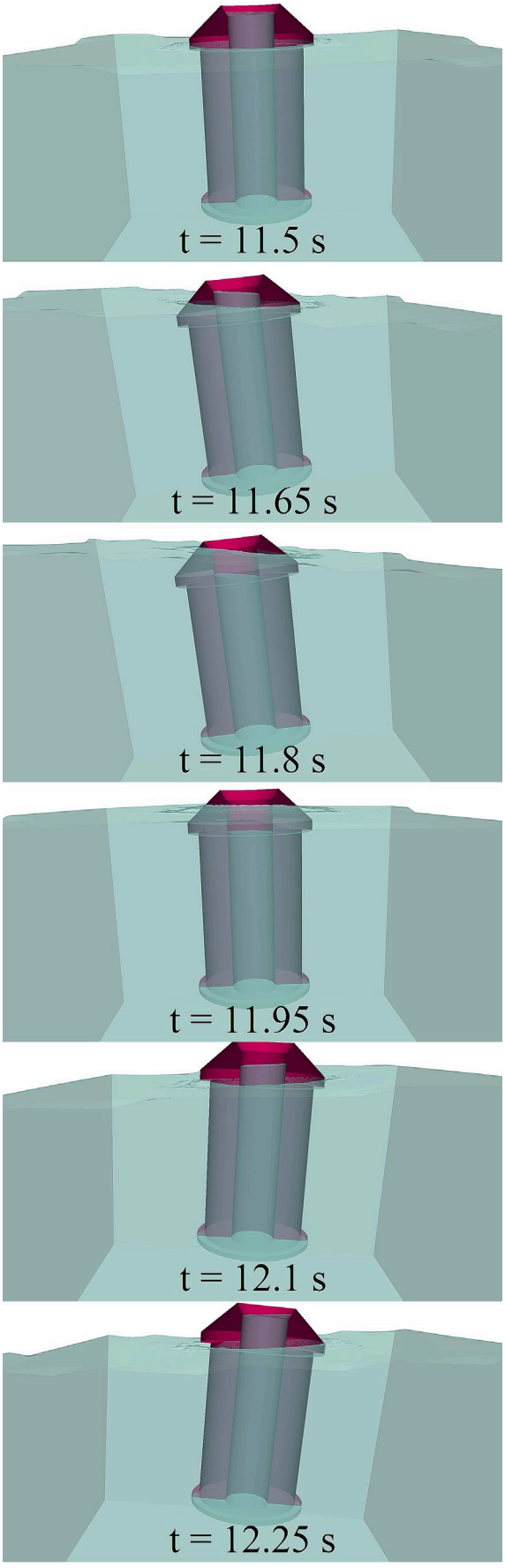

Fig. 25. CFD simulation at different time steps showing the moonpool oscillations for the CoM_2 prototype for the TW2 test case.

7. Conclusions

This paper presented the hydrodynamic analysis and optimization of a new axisymmetric single cylindrical Wave Energy Converter (WEC) with a moonpool at its centre, called MoonWEC, using a Numerical Wave Tank (NWT) in OpenFOAM®, where the conditions obtained during the original laboratory experiments were numerically reproduced and validated. The overInterDyMFoam solver in OpenFOAM was used for the multiphase rigid body dynamics, coupled with a dynamic mooring library called MooDy to model the mooring chains. A reduced-scale prototype of the MoonWEC on a scale of 1:64 and the NWT dimensions representing a portion of the experimental wave flume were used. The results of the free surface elevations and the floating body motions from the CFD model matched the data obtained from the laboratory experiments.

The first part of this paper focused on the laboratory experiments, including a free decay test where the prototype was released from a given positive excitation in heave and six wave-structure interaction (WSI) tests. Qualitative and quantitative data for the motion of the prototype were recorded with a GoPro camera, while quantitative data for the free surface were acquired using multiple resistive-type wave gauges. The results showed that the prototype has good potential for energy conversion in heave, with RAO values greater than 1, indicating that the device can be excited even more than the exciting wave.

The second part of this paper focused on the development and validation of the NWT by numerically reproducing the physical experiments. The cell size of the mesh was optimized to reduce computational costs. Qualitative analysis was performed by comparing numerical scenarios with physical images. Quantitative analysis was performed by comparing heave and pitch responses in time, and heave and pitch spectra. Good agreement between experimental and numerical data was observed throughout all the simulations. In the free decay test, a difference of 1.29% and 1.08% was observed for the natural periods in heave and pitch, respectively. For the wave structure interaction, larger differences were detected (12.54%, 10.81% and 6.66%) for the less energetic cases (R01, R02 and R03), and smaller differences (3.57%, 1.18% and 2.61%) for the more energetic cases (R04, R05, R06).

The third part of this paper focused on the main objective of the study, which is to numerically optimize the heave, pitch and moonpool motion of the MoonWEC. The pitch motion was observed to be excessively high during the experimental campaign, which hindered the vertical oscillations of the moonpool. To reduce the pitch motion of the MoonWEC when interacting with waves, two virtual numerical prototypes (CoM_2 and CoM_3) were created by shifting the centre of mass. Shifting the centre of mass did not affect the heaving period of the device, but it drastically changed the pitching period. For a wave period of 0.75 s, shifting the centre of mass down (by 15.62 mm) amplified the pitch motion by 3 times, while shifting the centre of mass up (by 15.38 mm) reduced the pitch motion by 3.5 times. The response of CoM_2 was studied further, and it was observed that for the given range of wave periods, it was able to keep the pitch rotations to a minimum while amplifying the heaving amplitudes. Considering the moonpool, it was found for the optimized prototype configuration (CoM_2) that the ratio between the moonpool oscillations and the wave amplitudes is sufficiently high, by a factor of 2.34, for the wave period corresponding to its natural period and there is a phase lag between the MoonWEC device and the moonpool oscillations.

This work confirms the capability of the CFD model in OpenFOAM coupled with the MooDy library to study and optimize the physical design of complex floating bodies accurately, as demonstrated by the successful example of the MoonWEC device.

Future work will focus on exploiting the NWT to analyse the survivability of the MoonWEC device under severe conditions and to study the damping caused by the inclusion of a power take-off (PTO).

Acknowledgements

The authors would like to acknowledge CINECA for providing high-performance computing resources that made it possible to run the CFD simulations in a timely manner. We also warmly thank technician Alberto Boninsegni for his laboratory support. Furthermore, we express our sincere gratitude to the anonymous reviewers for their insightful and constructive comments. The project was funded under the National Recovery and Resilience Plan (NRRP), Mission 04

Component 2 Investment 1.5 - NextGenerationEU, Call for tender n. 3277 ECOSISTER dated 30/12/2021 (Award Number: 0001052 dated 23/06/2022).

References

Aalbers, A.B., 1984. The water motions in a moonpool. Ocean Engineering 11, Issue 6, 557–579.

Aliyar, S., Ducrozet, G., Bouscasse, B., Bonnefoy, F., Sriram, V., Ferrant, P., 2022. Numerical coupling strategy using HOS-OpenFOAM-MoorDyn for OC3 Hywind SPAR type platform. Ocean Engineering 263, 112206.

Altomare, C., Gironella, X., 2014. An experimental study on scale effects in wave reflection of low-reflective quay walls with internal rubble mound for regular and random waves. Coastal Engineering, 90, 51-63.

Alves, M.A., Costa, I.R., Sarmento, A.J., Chozas, J.F., 2010. Performance evaluation of an axisymmetric floating OWC. In: The Twentieth International Offshore and Polar Engineering Conference, OnePetro.

Antonini, A., Gaeta, M.G., Lamberti, A., 2012. Wave—Induced devices for the oxygenation of deep layer: A physical investigation. Coastal Engineering, 2.

Antonini, A., Lamberti, A., Archetti, R., 2015. OXYFLUX, an innovative wave-driven device for the oxygenation of deep layers in coastal areas: A physical investigation. Coastal Engineering 104, 54–68.

Antonini, A., Lamberti, A., Archetti, R., Miquel, A.M., 2016. CFD investigations of OXYFLUX device, an innovative wave pump technology for artificial downwelling of surface water. Applied Ocean Research 61, 16–31.

Antonini, A., Lamberti, A., Archetti, R., Miquel, A.M., 2016. Dynamic overset RANS simulation of a wave-driven device for the oxygenation of deep layers. Ocean Engineering 127, 335–348.

Barajas, G., Lara, J.L., Di Paolo, B., Losada, I.J., 2022. Analysis of a floating wave energy converter interaction with waves using the Overset framework. In: Proceedings of the 9th International Conference on Computational Methods in Marine Engineering (Marine 2021), Edinburg, Scotland.

Barreira, R., Sphaier, S.H., Masetti, I.Q., Costa, A.P., Levi, C., 2005. Behavior of a mono-column structure (monobr) in waves. In: International Conference on Offshore Mechanics and Arctic Engineering, 41960, 867-873.

Barooni, M., Ashuri, T., Velioglu Sogut, D., Wood, S., Ghaderpour Taleghani, S., 2022. Floating Offshore Wind Turbines: Current Status and Future Prospects. Energies, 16(1), 2.

Benites-Munoz, D., Huang, L., Anderlini, E., Marín-Lopez, J.R., Thomas, G., 2020. Hydrodynamic Modelling of An Oscillating Wave Surge Converter Including Power Take-Off. Journal of Marine Science and Engineering 8, 771.

Brown, S.A., Ransley, E. J., Greaves, D. M., 2021. Assessing focused wave impacts on floating wave energy converters using OpenFOAM. In: Proceedings of the Institution of Civil Engineers – Engineering and Computational Mechanics, 174(1), 4-18.

Chandar, D.D., 2019. On overset interpolation strategies and conservation on unstructured grids in OpenFOAM. Computer Physics Communications, 239, 72-83.

Chen, H., Hall, M, 2022. CFD simulation of floating body motion with mooring dynamics: Coupling MoorDyn with OpenFOAM. Applied Ocean Research 124, 103210.

Chen, H., Qian, L., Ma, Z., Bai, W., Li, Y., Causon, D., Mingham, C., 2019. Application of an overset mesh-based numerical wave tank for modelling realistic free-surface hydrodynamic problems. Ocean Engineering, 176, 97-117.

Chen, J., Zhang, J., Wang, G., Zhang, Q., Guo, J., Sun, X., 2022. Numerical simulation of the wave dissipation performance of floating box-type breakwaters under long-period waves. Ocean Engineering 266, Part 4, 113091.

Davidson, J., Karimov, M., Szelechman, A., Windt, C., Ringwood, J., 2019. Dynamic mesh motion in OpenFOAM for wave energy converter simulation. In: Proceedings of the 14th OpenFOAM Workshop, Duisburg, Germany.

Di Paolo, B., Lara, J.L., Barajas, G., Paci, A., Losada, I.J., 2018. Numerical analysis of wave and current interaction with moored floating bodies using overset method. In: International Conference on Offshore Mechanics and Arctic Engineering, Vol. 51210, p. V002T08A037, American Society of Mechanical Engineers.

Drew, B., Plummer, A.R., Sahinkaya, M.N., 2009. A review of wave energy converter technology. In: Proceedings of the Institution of Mechanical Engineers, Part A: Journal of Power and Energy, 223(8), 887–902.

Duckers, L, 2004. Wave energy, in: G. Boyle (Ed.), Renewable energy. Oxford University Press, Oxford, UK, 2nd edition, ch. 8.

Erdinç, O., Paterakis, N.G., Catalão, J.P.S., 2015. Overview of insular power systems under increasing penetration of renewable energy sources: Opportunities and challenges. Renewable and Sustainable Energy Reviews, 52, 333-346.

Eskilsson, C.G., Palm, J., Bergdahl, L., 2017. On numerical uncertainty of VOF-RANS simulations of wave energy converters through V&V technique. In: Proceedings of the 12th European Wave and Tidal Energy Conference, p. 18, Cork, Ireland.

Falcão, A.F.D.O., 2010. Wave energy utilization: A review of the technologies. Renewable and sustainable energy reviews, 14(3), 899-918.

Gaeta, M.G., Segurini, G., Miquel, A.M., Archetti, R., 2020. Implementation and Validation of a Potential Model for a Moored Floating Cylinder under Wave. Journal of Marine Science and Engineering 8, 131.

Göteman, M., 2017. Wave energy parks with point-absorbers of different dimensions. Journal of Fluids and Structures, 74, 142–157.

Guo, B., Wang, T., Jin, S., Duan, S., Yang, K., Zhao, Y., 2022. A Review of Point Absorber Wave Energy Converters. Journal of Marine Science and Engineering, 10(10), 1534.

Hall, M., 2020. MoorDyn V2: New Capabilities in Mooring System Components and Load Cases: Preprint. Golden, CO: National Renewable Energy Laboratory. NREL/CP5000-76555.

Higuera, P., Lara, J.L., Losada, I.J., 2013. Realistic wave generation and active wave absorption for Navier–Stokes models: Application to OpenFOAM®. Coastal Engineering 71, 102–118.

Hirt, C.W., Nichols, B.D., 1981. Volume of fluid (VOF) method for the dynamics of free boundaries. Journal of Computational Physics 39, Issue 1, 201–225.

Islam, H., Mohapatra, S.C., Gadelho, J., Soares, C.G., 2019. OpenFOAM analysis of the wave radiation by a box-type floating structure. Ocean Engineering 193, 106532.

Iturrioz, A., Guanche, R., Lara, J.L., Vidal, C., Losada, I.J., 2015. Validation of OpenFOAM® for oscillating water column three-dimensional modeling. Ocean Engineering, 107, 222-236.

Jasak, H., 1996. Error Analysis and Estimation for the Finite Volume Method with Applications to Fluid Flows (Doctoral dissertation). Department of Mechanical Engineering, Imperial College of Science, Technology and Medicine. Imperial College London (University of London).

Jiang, S.C., Bai, W., Yan, B., 2021. Higher-order harmonic induced wave resonance for two side-by-side boxes in close proximity. Physics of Fluids, 33(10), 102113.
Jiang, S., Tang, P., Zou, L., Liu, Z., 2017. Numerical simulation of fluid resonance in a moonpool by twin rectangular hulls with various configurations and heaving amplitudes. Journal of Ocean University of China 16, 422–436.
Katsidoniotaki, E., Göteman, M., 2022. Numerical modelling of extreme wave interaction with point-absorber using OpenFOAM. Ocean Engineering, 245, 110268.
Larsen, B., Fuhrman, D., 2018. On the over-production of turbulence beneath surface waves in Reynolds-averaged Navier–Stokes models. Journal of Fluid Mechanics, 853, 419-460.
Li, Y., Fuhrman, D., 2022. On the turbulence modelling of waves breaking on a vertical pile. Journal of Fluid Mechanics, 953, A3.
Mia, M.R., Zhao, M., Wu, H., 2023. Effects of heave motion of an elastically supported floating oscillating water column device on wave energy harvesting efficiency. Physics of Fluids, 35(1), 017115.
Mardani, A., Jusoh, A., Zavadskas, E.K., Cavallaro, F., Khalifah, Z., 2015. Sustainable and Renewable Energy: An Overview of the Application of Multiple Criteria Decision-Making Techniques and Approaches. Sustainability 7, 13947-13984.
Miquel, A.M., Archetti, R., 2019. New MoonWEC concept and its device optimization. In: Proceedings of the 13th European Wave and Tidal Energy Conference (EWTEC 2019), Naples, Italy.
Miquel, A.M., Archetti, R., 2020. Dispositivo di generazione di energia elettrica dal moto ondoso. IT. Patent No. 102017000134759. Ufficio Italiano Brevetti e Marchi, 11.2.2020.
Miquel, A.M., Lamberti, A., Antonini, A., Archetti, R., 2020. The MoonWEC: a new technology for wave energy conversion in the Mediterranean Sea. Ocean Engineering 217, 107958.
OpenFOAM® User Guide, URL: https://www.openfoam.com/documentation/user-guide
Palm, J., 2017. Mooring Dynamics for Wave Energy Applications (Doctoral dissertation). Chalmers University of Technology.
Palm, J., Eskilsson, C., 2018. MOODY User Manual: version 1.0.0. Chalmers University of Technology, Department of Mechanics and Maritime Sciences.
Palm, J., Eskilsson, C., Bergdahl, L., 2017. An hp-adaptive discontinuous Galerkin method for modelling snap loads in mooring cables. Ocean Engineering, 144, 266-276.
Palm, J., Eskilsson, C., Paredes, G.M., Bergdahl, L., 2016. Coupled mooring analysis for floating wave energy converters using CFD: Formulation and validation. International Journal of Marine Energy 16, 83–99.
Pelc, R., Fujita, R.M., 2002. Renewable energy from the ocean. Marine Policy, 26(6), 471–479.
Peng, N.N., Lau, W.K., Wai, O.W. H., Chow, K.W., 2023. Computational and experimental studies of wave–structure interaction: Wave attenuation by a floating breakwater. Physics of Fluids, 35(4), 045112.
Pinguet, R., Benoit, M., Molin, B., Rezende, F., 2022. CFD analysis of added mass, damping and induced flow of isolated and cylinder-mounted heave plates at various submergence depths using an overset mesh method. Journal of Fluids and Structures, 109, 103442.
Power buoys: How the sea stands a good chance against sun and wind, 19 May 2001. The Economist. Retrieved from https://www.economist.com/science-and-technology/2001/05/17/power-buoy
Ran, Z., Kim, M.H., Niedzwecki, J.M., Johnson, R.P., 1996. Responses of a spar platform in random waves and currents (experiment vs. theory). International Journal of Offshore and Polar Engineering, 6(01).
Romano, A., Lara, J.L., Barajas, G., Di Paolo, B., Bellotti, G., Di Risio, M., Losada, I.J., De Girolamo, P., 2020. Tsunamis generated by submerged landslides: numerical analysis of the near-field wave characteristics. Journal of Geophysical Research: Oceans, 125(7), e2020JC016157.
Rusche, H., 2002. Computational fluid dynamics of dispersed two-phase flows at high phase fractions (Doctoral dissertation). Department of Mechanical Engineering, Imperial College of Science, Technology and Medicine. Imperial College London (University of London).
Sheng, W., Flannery, B., Lewis, A., Alcorn, R., 2012. Experimental studies of a floating cylindrical OWC WEC. In: International Conference on Offshore Mechanics and Arctic Engineering, Vol. 44946, pp. 169–178, American Society of Mechanical Engineers.
Singh, U., Abdussamie, N., Hore, J., 2020. Hydrodynamic performance of a floating offshore OWC wave energy converter: An experimental study. Renewable and Sustainable Energy Reviews, 117, 109501.
Sjökvist, L., Göteman, M., 2016. The effect of overtopping waves on peak forces on a point absorbing WEC. In: Proceedings of the Asian Wave and Tidal Energy Conference Series AWTEC, pp. 24–28, Singapore.
Song, Z., Lu, L., Cheng, L., Liu, Y., Tang, G., Lou, X., 2022. Fully nonlinear numerical investigations on the dynamics of fluid resonance between multiple bodies in close proximity. Physics of Fluids, 34(12), 122106.
Sphaier, S.H., Torres, F.G.S., Masetti, I.Q., Costa, A.P., Levi, C., 2007. Monocolumn behavior in waves: experimental analysis. Ocean Engineering, 34(11-12), 1724-1733.
Stagonas, D., Warbrick, D., Muller, G., Magagna, D., 2011. Surface tension effects on energy dissipation by small-scale, experimental breaking waves. Coastal Engineering, 58(9), 826-836.
Stern, F., Wilson, R.V., Coleman, H.W., Paterson, E.G., 2001. Comprehensive approach to verification and validation of CFD simulations—part 1: methodology and procedures. J. Fluids Eng., 123(4), 793-802.
Tan, L., Cheng, L., Ikoma, T., 2021. Damping of piston mode resonance between two fixed boxes. Physics of Fluids, 33(6), 062117.
Thorpe, T.W., 1999. A brief review of wave energy. Technical report no. R120, Energy Technology Support Unit (ETSU), A report produced for the UK Department of Trade and Industry.
Utsunomiya, T., Matsukuma, H., Minoura, S., Ko, K., Hamamura, H., Kobayashi, O., Sato, I., Nomoto, Y., Yasui, K., 2013. On-sea experiment of a hybrid spar for a floating offshore wind turbine using a 1/10 scale model. Journal of Offshore Mechanics and Arctic Engineering, 135(3).
Vissio, G., 2017. ISWEC toward the sea – Development, Optimization and Testing of the Device Control Architecture (Doctoral dissertation). Politecnico di Torino.
Vukčević, V., 2016. Numerical modelling of coupled potential and viscous flow for marine applications (Doctoral dissertation). Faculty of Mechanical Engineering and Naval Architecture, University of Zagreb.
Wang, C., Zhang, Y., 2021. Numerical investigation on the wave power extraction for a 3D dual-chamber oscillating water column system composed of two closely connected circular sub-units. Applied Energy, 295, 117009.
Wang, C., Zheng, S., Zhang, Y., 2022. A heaving system with two separated oscillating water column units for wave energy conversion. Physics of Fluids, 34(4), 047103.
Wang, X., Zhou, J.F., 2020. Numerical and experimental study on the scale effect of internal solitary wave loads on spar platforms. International Journal of Naval Architecture and Ocean Engineering, 12, 569-577.
Weber, J., Costello, R., Ringwood, J.V., 2013. WEC technology performance levels (TPLs)-metric for successful development of economic WEC technology. In: Proceedings of the 10th European Wave and Tidal Energy Conference (EWTEC2013), Aalborg, Denmark.

Weller, H.G., 2002. Derivation, modelling and solution of the conditionally averaged two-phase flow equations. Technical Report TR/HGW/02. Nabla Ltd.

Windt, C., Davidson, J., Chandar, D.D., Faedo, N., Ringwood, J.V., 2020. Evaluation of the overset grid method for control studies of wave energy converters in OpenFOAM numerical wave tanks. Journal of Ocean Engineering and Marine Energy, 6(1), 55-70.

Windt, C., Davidson, J., Schmitt, P., Ringwood, J.V., 2019. On the assessment of numerical wave makers in CFD simulations. Journal of Marine Science and Engineering, 7(2), 47.

Wu, T., Luo W., Jiang D., Deng R., Huang S., 2021. Numerical Study on Wave-Ice Interaction in the Marginal Ice Zone. Journal of Marine Science and Engineering 9, 4.

Xu, C., Huang, Z., 2019. Three-dimensional CFD simulation of a circular OWC with a nonlinear power-takeoff: Model validation and a discussion on resonant sloshing inside the pneumatic chamber. Ocean Engineering, 176, 184-198.

Zabihi, M., Mazaheri, S., Rezaee Mazyak, A., 2017. Wave generation in a numerical wave tank. International Journal of Coastal, Offshore and Environmental Engineering, 2(4), 33-43.

Zelt J.A., Skjelbreia J.E., 1992. Estimating Incident and Reflected Wave Fields Using an Arbitrary Number of Wave Gauges. In: Proceedings of the 23rd International Conference on Coastal Engineering, Venice, Italy.

Appendix A

Table A.1
Summary of the boundary conditions used in the OpenFOAM CFD model.

Boundary	Parameters				
	alpha.water	U	zoneID	p_rgh	
inlet	zeroGradient	waveVelocity	zeroGradient	fixedFluxPressure	
outlet	zeroGradient	waveVelocity	zeroGradient	fixedFluxPressure	
ground	zeroGradient	fixedValue	zeroGradient	fixedFluxPressure	
walls	zeroGradient	slip	zeroGradient	fixedFluxPressure	
atmosphere	inletOutlet	pressureInletOutletVelocity	zeroGradient	totalPressure	
MoonWec	zeroGradient	movingWallVelocity	zeroGradient	fixedFluxPressure	
oversetPatch	overset	overset	overset	overset	
oversetSides	overset	overset	overset	patchType	overset
				type	fixedFluxPressure
Boundary	Parameters				
	k	omega	nut	pointDisplacement	
inlet	zeroGradient	zeroGradient	calculated	fixedValue	
outlet	zeroGradient	zeroGradient	calculated	fixedValue	
ground	kqRWallFunction	omegaWallFunction	nutkWallFunction	fixedValue	
walls	slip	slip	slip	fixedValue	
atmosphere	inletOutlet	inletOutlet	calculated	fixedValue	
MoonWec	kqRWallFunction	omegaWallFunction	nutkWallFunction	calculated	
oversetPatch	overset	overset	overset	patchType	overset
				type	zeroGradient
oversetSides	overset	overset	overset	patchType	overset
				type	zeroGradient

Table A.2
Summary of physical properties of the two fluids used in the OpenFOAM CFD model.

Parameter		Value	Unit
Acceleration due to Gravity g		9.81	m/s^2
Water	Density ρ_w	998.20	kg/m^3
	Kinematic Viscosity ν_w	1.00×10^{-6}	m^2/s
Air	Density ρ_a	1.00	kg/m^3
	Kinematic Viscosity ν_a	1.48×10^{-5}	m^2/s
Surface Tension σ		0.07	N/m